3-D Numerical Simulations on Flow and Mixing Behaviors in Gas–Liquid–Solid Microchannels

Tang Can
School of Chemical Engineering and Technology, Tianjin University, Tianjin 300072, P.R. China

Liu Mingyan
School of Chemical Engineering and Technology, Tianjin University, Tianjin 300072, P.R. China

Stake Key Laboratory of Chemical Engineering, Tianjin 300072, P.R. China

Xu Yonggui
School of Chemical Engineering and Technology, Tianjin University, Tianjin 300072, P.R. China

DOI 10.1002/aic.13980
Published online March 7, 2013 in Wiley Online Library (wileyonlinelibrary.com)

Three-dimensional (3-D) gas-liquid–solid flow and mixing behaviors in microchannels were simulated by coupled volume of fluid and discrete phase method and simulations were validated against observations. The detachment time and length of gas slug are shortened in liquid–solid flow, compared with those in liquid flow due to higher superficial viscosity of liquid–solid mixture, which will move the bubble formation toward the dripping regime. Solid particles mainly distribute in liquid slug and particle flow shows obvious periodicity. With the increase of contact angle of the inner wall, gas slug (0–50°), stratified (77–120°), and liquid drop (160°) flows are observed. The residence time distributions of solid and liquid phases are similar because particles behave as tracers. The backmixing of solid and liquid phases in liquid drop flow is the weakest among the three flow patterns, and the backmixing of gas phase in slug flow is weaker than that in both stratified and liquid drop flows. The results can provide a theoretical basis for the design of microreactors. © 2013 American Institute of Chemical Engineers *AIChE J*, 59: 1934–1951, 2013
Keywords: bubble phenomena, multiscale simulation, multiphase flow, microfluidics, mixing

Introduction

According to the standard of the First International Conference on Microchannels and Minichannels, the characteristic scale of micro- and minichannels ranges from 10×10^{-6} m to $3{,}000 \times 10^{-6}$ m. The surface area of microscale systems can reach 10,000–50,000 m^2/m^3, which is much higher than that of macroscale systems (usually less than 1,000 m^2/m^3).[1] For this reason, microscale systems can enhance mass and heat-transfer processes compared to macroscle systems.[2,3] Microchannel systems are encoutered in many important industrial applications such as microchannel heat exchangers, microreactors and other microdevices.[4] These microscale equipments have several advantages such as easiness to scale-up, operation at constant temperature and safe process. Hence, microchannels can be widely applied in chemical, pharmacy, biology, medicine and electronics industries.[5]

With the development of computational science, computational fluid dynamics (CFD) becomes a powerful tool for studying the flow, mass and heat transfer in multiphase systems. Compared to experimental study, CFD simulation is more economical and flexible. Hence, it is also widely used in the study of flow, mass and heat transfer in microchannels.

A few researchers focused on the studies of gas-liquid and liquid-liquid two-phase flows in microchannels. Liu et al.[6] divided gas-liquid flow in microchannels into five different flow regimes, bubble, bubble-slug, slug (Taylor), churn and annular flows. A high-speed camera was widely used for flow pattern observations in microchannels.[7] Flow regime transforms with flow parameters, such as superficial gas or liquid velocity,[8,9] and some dimensionless groups, such as Webber number (We) and Reynolds number (Re) were employed to characterize the flow regimes.[10,11] However, a well-accepted flow regime map has not been founded due to the complexities of the scale and structure of microchannels and fluids used. Flow patterns are closely related to the formation mechanisms of bubble and droplet, which can be distinguished by the capillary number of continuous phase.[12,13]

From the observation of the flow pattern map, it can be found that slug flow occupies the majority area of the map and it is the most important one.[14] A few researchers focused on the study of slug flow in microchannels with both numerical and experimental methods. Qian and Lawal[15] simulated slug flow in gas-liquid microchannels with a T-junction, and the effects of operation conditions and liquid properties on the length of gas slug were studied. They found that the slug length was the function of the channel

Correspondence concerning this article should be addressed to Liu Mingyan or Liu M. Y. at myliu@tju.edu.cn.

width, void fraction (Re), capillary number (Ca). Unfortunately, the thin liquid film between the slug and the wall was not captured because of the coarse mesh. According to the liquid film thickness equation proposed by Bretherton,[16] Gupta et al.[17] refined the mesh in the region near the wall of microchannel and successfully captured the liquid film. Asadolahi et al.[18] simulated the hydrodynamics and heat transfer in a unit cell in Taylor flow with the method of dynamic meshes. For fully developed flow, simulation with dynamic mesh could save considerable computational source. Kumar et al.[19] and Kashid et al.[20] simulated the hydrodynamics of slug flow in curved and Y-shape microchannels, respectively. It was found that liquid and/or gas slug length depended on the geometry condition of the inlet, operating condition and the wettability of the inner wall of the microchannel. Two-dimensional (2-D) and 3-D simulations for bubble generation in microchannels were compared by Goel and Buwa, and the results showed that 2-D solution was not grid independence because the Laplace pressure between the interfaces of bubble could not be simulated correctly.[21] Taha and Cui[22,23] simulated the circulation of vortex in liquid slug and found that the vortex became smaller with the incensement of Ca number.

Garstecki et al.[24] experimentally investigated the generation process of Taylor bubble and liquid slug and divided the process into four stages, (1) the tip of the discontinuous phase entered the main channel, (2) the growing droplet and bubble spanned the whole cross section of the main channel, (3) the droplet and bubble elongated in the downstream direction and the neck connecting it to the inlet thinned, and (4) the neck broke, the disconnected droplet and bubble flowed downstream and the tip of the discontinuous phase recoiled back toward the inlet. Based on the experimental results, an equation to calculate the length of immiscible slug was proposed, and the length of immiscible slug depended on the ratio of Q_c (flow rate of continuous phase) to Q_d (flow rate of discontinous phase) and geometry of microchannels. Sobieszuk et al.[25] measured the length of Taylor bubble in microchannels with a Y-junction, the experimental results agreed well with the calculation values with Qian and Lawal's[15] equations. The velocity filed around the discontinuous phase during the formation of a slug or drop was measured by an effective tool of microparticle image velocimetry (μ-PIV).[26,27] Optical testing technology was also applied in microfluidics measurements. γ-ray computed tomography (CT) was used to study gas and liquid holdup distributions in microchannels,[28] and NMR microimaging was applied to explore flow characteristics in complicated shaped channels.[29] Additionally, the study of two immiscible phase flow in microchannels was extended to three-phase. Wang et al.[30] investigated gas-liquid-liquid flow in microchannels with two T-junctions, size laws and the distributions of the bubbles and droplets were investigated.

Mass transfer of gas-liquid flow in microchannels is an important issue in the processes of reaction, mixing, absorption and extraction. Numerical simulations on the characteristics of mass transfer of gas-liquid flow in microchannels have been carried out recently and the results showed that the efficiency of mass transfer in microchannels could be improved one- to two-orders of magnitude compared with macrosystem.[31–34] Abiev and Lavrestov[35] experimentally compared the performance of mass transfer from solid wall to the liquid bulk between gas-liquid flow and homogeneous flow and found that mass flow was intensified by Taylor circulations. Heat transfer of gas-liquid flow in microchannels was also investigated, it was found that the ratio of the Nusselt number to that of flow of pure liquid was always greater than 1.0 and ranged from 1.9 to 3.3.[36] In Mehdizadeh's work,[37] the ratio could even reach 6.1, i.e., heat transfer of gas-liquid flow was enhanced obviously compared with pure liquid flow in microchannels. He et al.[38] compared heat transfer of wet slug and dry slug flow in microchannels, and heat-transfer enhancement was obtained mainly due to the presence of the thin liquid film.

Gas-liquid and liquid-liquid two-phase flows in microchannels have been applied in engineering. For gas-liquid flow, it was widely encountered in fuel cells. Gas phase was treated as continuous phase, while liquid phase which was treated as discontinuous phase entered into the microchannels from the side walls. The VOF numerical method was used to simulate the situation that water which was generated from electrode reaction in the fuel cell entered into the main channel from porous diffusion layer. The investigations showed that the size, structure and material of microchannels could be properly chosen to avoid flooding in the fuel cells.[39–41] For liquid-liquid flow in microchannels, it was mainly applied in the preparation of emulsion droplet in micromixers. Micromixers show advantages such as high efficiency, safety and flexibility to control in many fields, e.g., chemistry, biology, materials and chemical engineering.[42,43] Applications of micromixers in multiphase flow and mixing process have significant meaning in developing microchemical technology. Kobayshi et al.[44,45] simulated the generation process of emulsion droplet in vertical microchannels. Meanwhile, influence of microchannels' size on this process was analyzed by investigating the pressure drop and size of the droplet.

For the study of multiphase flow with solid particles in microchannels, it focused mainly on the gas–solid or liquid–solid flow. Ookawara et al.[46] simulated the particle concentration distribution in curved microchannels for gas–solid flow. The simulation results showed that the particles of smaller size concentrated near the inner wall, while the bigger particles mainly distributed near the outer wall. Thus, the separation of particles with different sizes could be achieved by microseparators. A single-particle transport condition in a ratchet-like microchannel was simulated by Cisne et al.[47] A dimensionless group named Stokes number (St) was defined, which meant the ratio between the time of response of the particle to the action of the fluid and the characteristic flow time. The value of St of particle decides whether the particle will flow with streamlines as a tracer or not. Particles transport in microchannels under electric or magnetic field was also investigated,[48,49] and the electric or magnetic field force is the dominant force which influences the transport of charged or magnetic particles. In these researches, Newton's second law was employed to conduct force analysis for particles. The velocity and motion trajectory of particles can be solved by the integration of Newton's second law.

s mentioned previously, gas-liquid and liquid-liquid two-phase flows in microchannels have been intensively studied in recent years, including flow, heat and mass transfer. Meanwhile, flows of particles in liquid or gas phase in microchannels were also simulated based on Eulerian or Lagrangian method.

In recent years, gas-liquid–solid at microscale has been applied in chemical synthesis in a microreactor, and solid particles play a role of granular catalyst in three-phase. Catalyst was fed into the microreactor in the form of slurry.[50,51] Gas-liquid–solid microreactors were used in fluorination,

chlorination, hydrogenation, sulfonation, and photooxidation, etc.[52–55] Meanwhile, gas-liquid–solid flow can be applied in the preparation of micron particles.[56] For example, Wang et al.[57] synthesized $CaCO_3$ particle in nanoscale by CO_2 and $Ca(OH)_2$ solution in a membrane dispersion minireactor. Ufer et al.[58] investigated the flow pattern of catalyst support material particles in a liquid-liquid capillary microreactor. It was found that the hydrophilicity or hydrophobicity of the particles would determine its flow characteristics. Xie[59] studied the effects of fine particles on gas-liquid mass transfer in microchannels, and the enhancement of mass transfer changed with holdup and categories of particles.

Gas-liquid–solid flow in microchannels shows a board application prospect. Compared with microreactors involving a coated catalyst, gas-liquid–solid contact model owes its convenience to use different kinds of catalysts in a flexible and efficient way by avoiding the catalyst removal.[60] However, its flow and mixing behaviors have not been investigated systematically. What's more, the rules obtained from macroscale systems for gas-liquid–solid flow[61–63] cannot be extended to microscale systems. The characteristic dimension of microscale systems is at micron level, and some certain forces which can be neglected at macroscale have a great influence on the flow in microscale systems. In microscale systems, forces which are in proportion to characteristic dimensions, such as gravitational force, inertia force and buoyancy do not play important roles. Reversely, viscous force and surface tension, which are in inverse proportion to characteristic dimension, exerts an obvious effect on flow characteristics in microchannels. Hence, there is a big difference between macroscale and microscale systems for three-phase flow. It is a key step to understand the gas-liquid–solid flow, especially the flow and mixing characteristics of solid particles in microchannels in order to provide a theoretical basis for designing microreactors with high efficiency. Hence, the effects of solid particles on hydrodynamics of gas and liquid slug flows and phase mixing characteristics were especially studied in this article.

This article is organized as follows. First numerical simulations were compared with experimental results to validate the simulations. Then the effects of operation conditions and wettability of inner walls on flow patterns were investigated. Third, the difference between gas-liquid and gas-liquid–solid flows at the same operation conditions was numerically researched, and the effects of solid particle properties on gas-slug behaviors were analyzed. Flow characteristics of solid particles in slug flow were discussed in detail. Finally, the residence time distributions (RTDs) of solid particles, liquid and gas phases in three flow patterns were compared by varying contact angles of microchannel inner walls.

Numerical Methods

Numerical simulations of gas-liquid–solid flow in microchannels were executed on the software platform of Fluent software (version 6.3) using coupled volume of fluid (VOF), and discrete phase method (DPM), where VOF was used to capture the interface between gas and liquid phases and DPM was employed to track particle path-line. It should be noted that the interaction between continuous and discrete phases is two-way coupling, i.e., the discrete phase can also influence the flow behavior of continuous phase.

VOF method [64]

Hydrodynamics of continuous media can be described by continuity and momentum equations. For a Newtonian fluid, these equations are written as follows

$$\frac{\partial \rho}{\partial t}+\nabla\cdot(\rho\vec{u})=0 \tag{1}$$

$$\frac{\partial(\rho\vec{u})}{\partial t}+\nabla\cdot(\rho\vec{u}\vec{u})=-\nabla p+\nabla\cdot\left\{\mu\left[\nabla\vec{u}+(\nabla\vec{u})^T\right]\right\}+\vec{F}_s+\vec{F}_d \tag{2}$$

where $\vec{F}_s$ is the surface tension force, and $\vec{F}_d$ is the reacting force from discrete phase. On the righthand side of Eq. 2, the gravity force term does not exist, as the gravity force was neglected in the simulations. Thus, it can be explained as follows.

The Eo number (see Eq. 3) represents the relative significance between the gravity force and surface tension.[65] If $Eo<0.84$, gravity force can be neglected.[4] For all cases in this work, $Eo<0.1$ ($\rho_{l+s}=998.2$ kg/m^3, $\rho_g=1.225$ kg/m^3, and $d_h=5\times10^{-4}$ m in this article). Hence, gravity force was not considered here

$$Eo=\frac{{d_h}^2 g\left(\rho_{l+s}-\rho_g\right)}{\sigma} \tag{3}$$

The interface between different phases is obtained by solving an advection equation[64]

$$\frac{\partial \alpha_q}{\partial t}+\vec{u_q}\cdot\nabla\alpha_q=0 \tag{4}$$

In Eq. 4, α_q denotes the volume fraction of the q^{th} phase. Eq. 4 does not solve the primary phase, and the volume fraction of primary phase was calculated by the following constraints

$$\sum_{q=1}^{2}\alpha_q=1 \tag{5}$$

A "single-fluid" phase which is shared by all phases was used in Eqs. 1 and 2. The bulk properties in Eqs. 1 and 2, such as density and viscosity, were determined from the volume-fraction weighted average of the properties of the two fluids

$$\rho(\vec{x},t)=\alpha(\vec{x},t)\rho_{l+s}+[1-\alpha(\vec{x},t)]\rho_g \tag{6}$$

$$\mu(\vec{x},t)=\alpha(\vec{x},t)\mu_{l+s}+[1-\alpha(\vec{x},t)]\mu_g \tag{7}$$

The surface tension force term in Eq. 2 was considered by applying the continuum surface force (CSF) model proposed by Brackbill et al.[66] In this model, the surface tension force was considered to be constant along the surface, and only the forces normal to the interface were considered. The surface tension force at the bubble-liquid interface was expressed as a volume force in the momentum equation using the divergence theorem. This volume force for gas and liquid phases is given by

$$F_s=\sigma\frac{\rho\kappa\nabla\alpha_1}{0.5\left(\rho_g+\rho_{l+s}\right)} \tag{8}$$

where κ is the curvature and $\hat{n}$ is the surface normal, which are given as

$$k=\nabla\cdot\hat{n},\hat{n}=\frac{\vec{n}}{|\vec{n}|},\vec{n}=\nabla\alpha_q, \tag{9}$$

When a cell is adjacent to the wall, then the surface normal is

$$\hat{n}=\hat{n}_w\cos\theta+\hat{t}_w\sin\theta$$

where $\hat{n}_w$ and $\hat{t}_w$ are the unit vectors normal and tangential to the wall, respectively. θ is the contact angle.

DPM method [67]

The trajectory of solid particles was calculated by integrating the force balance on the solid particle, which is written in the form of Newton's second law in a Lagrangian reference frame

$$\frac{d\vec{u_p}}{dt}=\sum\vec{F}_{ext} \tag{10}$$

where $\vec{u_p}$ represents the velocity vector of solid particles, and $\vec{F}_{ext}$ represents all external force vectors exerted on the solid particle.

$\vec{F}_{ext}$ mainly includes drag force. The Saffman, Basset, Magnus and added forces were negligible in comparison with the fluidic drag force[49]

$$\vec{F_D}=\frac{18\mu_{l+s}}{\rho_p{d_p}^2}\frac{C_D\mathrm{Re}_p}{24}\left(\vec{u}_{l+s}-\vec{u_p}\right) \tag{11}$$

where ρ_p denotes the solid particle density ($\rho_p = 1050$ kg/m^3 in this article), and d_p denotes the diameter of solid particles ($d_p = 8 \times 10^{-6}$ m in this article). C_D is drag coefficient, and Re_p is the Reynolds number of solid particles

$$\mathrm{Re}_p=\frac{\rho d_p|\vec{u_p}-\vec{u}_{l+s}|}{\mu_{l+s}} \tag{12}$$

For micron solid particles, the drag coefficient C_D can be calculated by Stokes' law because Re_p is far smaller than 1.0 here

$$C_D=\frac{24}{\mathrm{Re}_p} \tag{13}$$

However, the buoyant force and Brownian motion were neglected when conducting force analysis for solid particles. In the calculations, the density of solid particles near equaled to that of liquid phase for simplicity; in such a manner, the particle weight was almost compensated by the buoyancy force exerted on the particle. The vector sum of buoyancy and gravity force (acceleration term, force/unit particle mass) can be written as

$$\vec{F}_{g+b}=(\rho_p\text{-}\rho_{l+s})\vec{g} \tag{14}$$

where $\vec{F}_{g+b}$ represents the vector sum of buoyancy and gravity forces.

Based on Eqs. 11 and 14, the ratio of $|\vec{F}_{g+b}|$ to $|\vec{F}_D|$ is of the order of 10^{-6}. Thus, both buoyancy and gravity forces were neglected in simulations. Brownian force influences the motion of solid particles obviously when the particle diameter is sufficiently small. Davison and Sharp[68] used a Peclet number defined as the ratio between u_p and Brownian diffusion coefficient (D_{Brownian}) to estimate the importance of Brownian motion

$$Pe=\frac{r_p u_p}{D_{Brownian}} \tag{15}$$

D_{Brownian} was calculated by the correlation proposed by Einstein.[69] The value of Pe calculated by Eq. 15 is of the order of 10^7. In Davison and Sharp's[68] work, $Pe = 460$, and Brownian motion was neglected in their analysis. In this article, Pe is much higher than that in the literature. Thus, the influence of Brownian motion was neglected for all cases.

In the DPM method, the holdup of solid particles (ε_p) was assumed to be sufficiently low that the effect of solid particles on the fluidic continuity equation and the inertia and stress terms in the momentum equation could be neglected, and only the reacting force from discrete phase was considered. In fact, the assumption can be accepted when the volume fraction of the discrete phase less than from 10 to 12%.[70] The two-way coupling was realized by the reacting force term in the momentum equation which represents the counter drag force exerted by solid particles.

Boundary conditions and numerical strategies

In simulations, the computational domain was usually smaller than the whole channel in order to save computational cost.[46,71] However, the length of inlet channels should be sufficiently long to ensure fully developed flow. This length can be determined by the correlation given by Dombrowski et al.[72]

$$\frac{L_e}{d_h}=0.379\exp\left(-0.148\mathrm{Re}\right)+0.055\mathrm{Re}+0.26 \tag{16}$$

This relationship was employed to determine the entrance length L_e of the inlet channels, where d_h is the hydraulic diameter of the channel ($d_h = 5 \times 10^{-4}$ m in this article). The Reynolds number in the inlet channel should be calculated based on the superficial velocity of single phase (v_{l+s} and v_g). In the case that $v_{l+s} = 0.17$ m/s, the corresponding $Re = 85$ and $L_e = 2.5 \times 10^{-3}$ m. The length of the main channel was designed as 7.5×10^{-3} m to ensure the flow regimes could be observed from the simulation results (Figure 1).

At the inlets, the velocity inlet was employed as the boundary condition, while at the outlet outflow was used as the boundary condition. The outflow boundary conditions were used to model flow exits where the details of the flow velocity and pressure were not known.[70] The computational domain is a part of the whole channel. Hence, the employing of outflow boundary condition is suitable for the simulation. The wetting properties of the inner wall were considered as a factor in the simulations. No-slip condition existed at the boundaries of the inner walls. However, the three-phase contact lines at the inner walls were moving. In order to avoid the stress singularities at the contact points, a Navier slip condition was often used.[73] In most applications, this slip length was expected to be much smaller than the mesh size used in the numerical computations.[74] In this work, the available computational resources did not allow the mesh size to be refined in such a way that the true slip length was captured correctly. Therefore, no explicit slip length was imposed. However, it should be noted that the algorithm itself introduced an implicit slip length on the order of the grid spacing.[74,75]

The computational domain was set filled with liquid initially (Figure 1), while solid particles distributed randomly

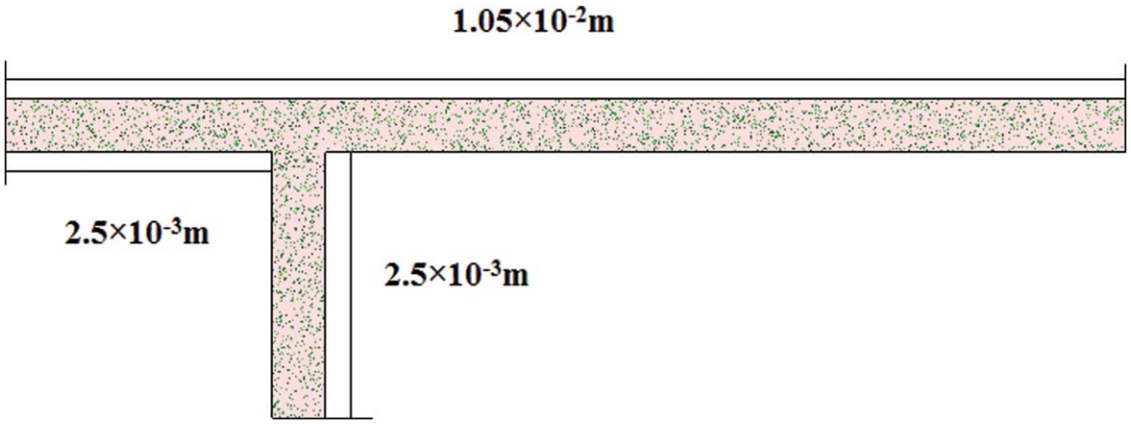

Figure 1. The initial condition in the computational domain of gas-liquid–solid flow in microchannel.

[Color figure can be viewed in the online issue, which is available at wileyonlinelibrary.com]

in the whole computational domain at a certain ε_p. Solid particles were injected into the channel with liquid, at the conditions that $v_{l+s} = 0.17$ m/s, $\varepsilon_p = 0.3\%$, and $d_p = 8 \times 10^{-6}$ m. The number of particles entering the computational domain per time step ($\Delta t = 5 \times 10^{-6}$ s) was 2.38 ($N_{p,\Delta t} = \frac{v_{l+s} \cdot \Delta t \cdot d_h^2 \cdot \varepsilon_p}{1/6 \pi \cdot d_p^3}$). In order to make the number of particles entering the computational domain to be a integer, particles were set to enter the computational domain from the liquid–solid suspensions inlet every 100 time steps. That is, 238 particles would enter the computational domain every 5×10^{-4} s, e.g., at 5×10^{-4} s (100th time step), 1×10^{-3} s (200th time step), 1.5×10^{-3} s (300th time step), and so on. Specifically, liquid–solid suspensions would move forward 8.5×10^{-5} m every 5×10^{-4} s (0.17 m/s $\times$ (5×10^{-4} s)), and 238 particles would appear in the (5×10^{-4}) $\times$ (5×10^{-4}) $\times$ (8.5×10^{-5}) m^3 domain close to the liquid–solid suspensions inlet randomly every 5×10^{-4} s (100 time steps).

Uncoupling arithmetic method was used to separate and to solve model equations. Pressure-velocity coupling was the pressure-implicit with splitting of operators (PISO) method. Pressure interpolation method was pressure staggering option (PRESTO), and momentum discretization method was QUICK model.

A courant number (Co) was used for the calculation of the volume fraction, which is defined as

$$Co = \frac{\Delta t}{\Delta x / u} \tag{17}$$

where Δx is the grid size, Δt is the time step, and u is the flow velocity.

In the VOF method, a maximum Co is usually set as 0.25.[17,76] The time step for continuous phase was set as 5×10^{-6} s to ensure the value of Co number was smaller than 0.25. However, the time step for solid particles was set as 5×10^{-7} s, for the reason that the diameter of particles was far smaller than the characteristic length of the channels (5×10^{-4} m).[77,78]

Studies of mesh size and grid independence

The effect of mesh size on the simulation results was examined by simulating the gas slug flow in liquid–solid systems. v_g was 0.85 m/s, v_{l+s} was 0.17 m/s, and ε_p was 0.3%. The grid size reduced approximately in equal proportion, and the reduction factor was equal to 0.5. Specially, the grid sizes were 5×10^{-5} m, 2.5×10^{-5} m and 1.25×10^{-5} m, respectively, and the corresponding numbers of grid points were 4.4×10^4, 2×10^5, and 1×10^6, respectively.

It should be noted that in order to capture the liquid film between the gas phase and the inner wall, the mesh near the inner wall was refined, as shown in Figure 2. The thickness of the liquid film was estimated by the correlation given by Bretherton[16]

$$\delta = 0.67 Ca^{2/3} d_h \tag{18}$$

where δ is the thickness of the liquid film, Ca is defined as[79]

$$Ca = \frac{\mu_{l+s}(v_{l+s} + v_g)}{\sigma} \tag{19}$$

At least five elements were needed across the refined area in order to capture the liquid film successfully.[17] In this case, the thickness of the liquid film was estimated to be 2×10^{-5} m. Therefore, a grid size of 4×10^{-6} m near the wall was set to try to capture the liquid film. Although Eq. 18 was proposed to calculate the thickness of the liquid film in gas-liquid flow, if liquid film could be captured, it could prove this refined meshing method to be reasonable.

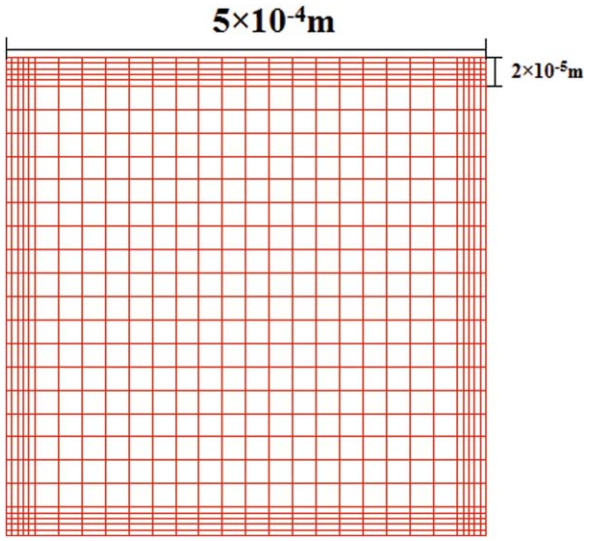

Figure 2. The cross section of the 2.5 × 10^{-5} m mesh.

[Color figure can be viewed in the online issue, which is available at wileyonlinelibrary.com]

Table 1. t_d and L_G at Different Meshes ($v_g = 0.85$m/s, $v_{l+s} = 0.17$m/s, $\sigma = 0.0728$N/m, $\varepsilon_p = 0.3\%$ and $\theta = 0°$)

Mesh size,10^{-5} m	5	2.5	1.25
t_d, 10^{-3} s	8.10	5.710	5.69
L_G, 10^{-3} m	5.031	3.566	3.631

In order to check whether these meshes can capture the liquid film or not, the wettability of the inner walls was set as completely hydrophilic, i.e., θ was 0°. The simulation results at different meshes are shown in Figure 3 and Table 1.

The detachment time (t_d) and the length of the first gas slug (L_G) were chosen as the inspection factors in the study of grid independence. As can be seen in Table 1, the two inspection factors scarcely change when the grid size is smaller than 2.5×10^{-5} m. It can be concluded that when the grid size is smaller than 2.5×10^{-5} m, the solution is grid independent. In order to save the computational time and to ensure that the solution is grid independent, the mesh with grid size 2.5×10^{-5} m was chosen in the simulations. In Cherlo's[71] work, the geometry size of the computational domain was $(5 \times 10^{-4}) \times (5.9 \times 10^{-4}) \times (2 \times 10^{-2})$ m^3, and the total number of grid points was 157,696. In this article, the total number of gird points is 200,480 and the geometry size of the computational domain is $(5 \times 10^{-4}) \times (5 \times 10^{-4}) \times (1.05 \times 10^{-2})$ m^3. The grid size is comparable to the one in Cherlo's work.[71] Besides, there exists an obvious liquid film between the gas slug and the inner wall in Figure 3, which proves that the liquid film was captured successfully with this meshing method.

Results and Discussion

Experimental validation

A set of visual experimental device was built to examine simulation results. The T-junction microchannel (custom-made, Wenchang Chip, P.R. China), was fabricated on a polymethyl methacrylate (PMMA) chip whose size was (5.9 $\times$ 10^{-2} m) $\times$ (2.8×10^{-2} m) $\times$ (3×10^{-3} m) (length $\times$ width $\times$ thickness) by precision milling, and consists of a main channel with overall length of 4×10^{-2} m, and a side channel with the length of 1×10^{-2} m. The cross area of the channels is a square, whose side length is 5×10^{-4} m. Three holes ($\Phi 1 \times 10^{-3}$ m), which were located at the points corresponding to the channels' ends, were punched on another PMMA chip with the same size as inlets and outlet of the microchannel. After these machining processes, the two PMMA chips were sealed together to assemble a microchannel by adhesive bonding technology. Figures 4 and 5 show the microchannel and its schematic map.

As shown in Figure 5, both gas and liquid–solid mixture were injected from 1×10^{-4} m^3 syringes by syringe pumps (PHD 22/2000, Harvard Apparatus, USA), and the syringes were connected to the inlets of the microchannel by Teflon

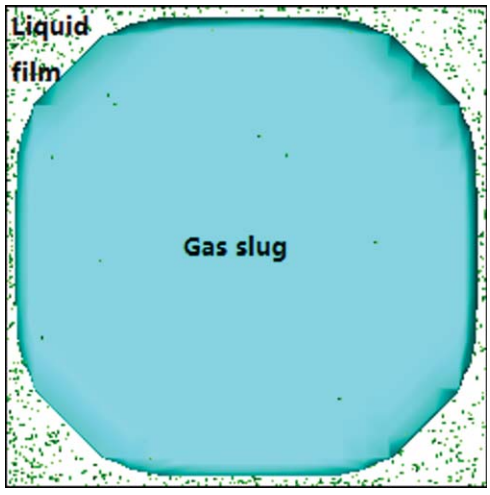

Figure 3. The liquid film at 2.5×10^{-5} m mesh ($v_g = 0.85$ m/s, $v_{l+s} = 0.17$ m/s, $\sigma = 0.0728$N/m, $\varepsilon_p = 0.3\%$ and $\theta = 0°$).

[Color figure can be viewed in the online issue, which is available at wileyonlinelibrary.com]

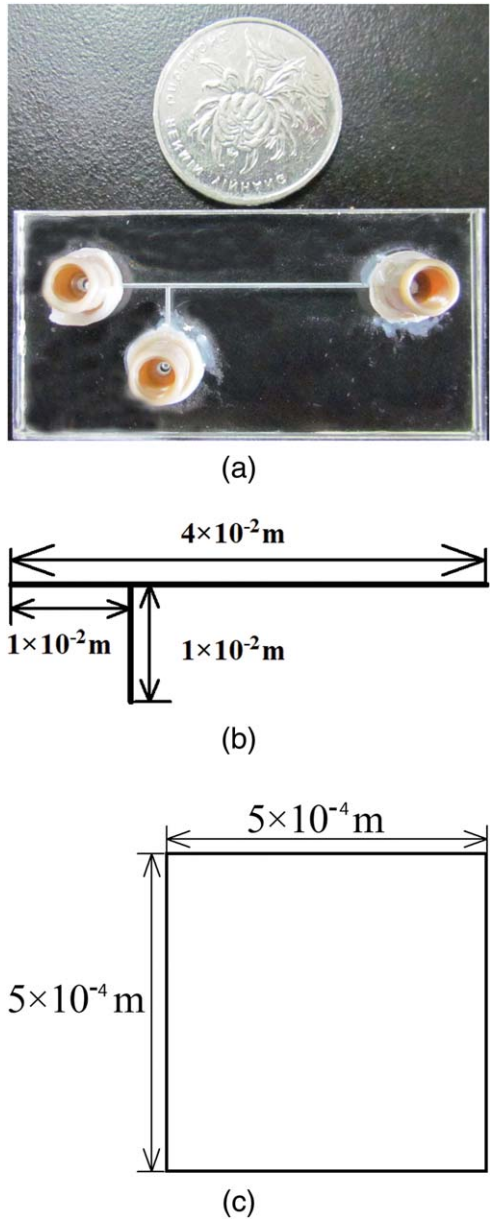

Figure 4. The microchannel and its schematic map.

(a) microchannel, (b) schematic map of microchannel, and (c) cross section. [Color figure can be viewed in the online issue, which is available at wileyonlinelibrary.com]

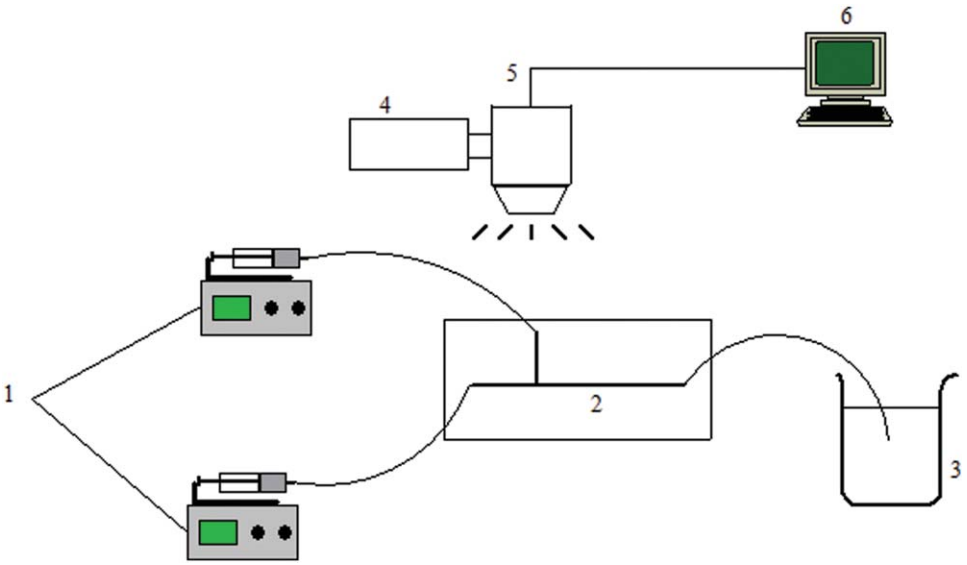

Figure 5. The schematic map of experiment procedure.

(1) Syringe pumps, (2) T-junction microchannel, (3) beaker, (4) high-speed camera, (5) microscope, and (6) PC. [Color figure can be viewed in the online issue, which is available at wileyonlinelibrary.com]

tubes with inner diameter (ID) of 2×10^{-3} m. The flow rates were controlled accurately by the control panels on the syringe pumps. Gas and liquid–solid mixtures were fed into the microchannel and began interacting with each other since the T-junction. Finally, they would spew into a beaker after exiting the microchannel. For this experiment, the microchannel was placed flatly on the objective table of an inverted microscope (Nikon Ti-S, Japan), which was equipped with a high-speed camera (Redlake Motion Pro Y-5, USA). The maximum shutter speed of the camera is 1/1,000,000 s. In this work, the frame rate was 1,000 fps. The flow snapshots at the T-junction convergence were captured simultaneously by the high-speed camera. Pictures were analyzed in postprocessing to quantify the size and the detachment time of the slugs. It should be noted that the detachment time of experiment was calculated by this method $t_d = \frac{t_{\text{overall}}}{N_s}$, where t_{overall} is the time between two snapshots shown the same flow status that the gas slug just broke up, and N_s is the number of gas slugs formed during this time.

In experiments, flow rates of gas and liquid–solid mixture corresponding to v_g and v_{l+s} (0.85 m/s and 0.17 m/s) were set as 2.125×10^{-7} m^3/s and 4.25×10^{-8} m^3/s, respectively. The superficial velocity of particles can be calculated by the product of v_{l+s} and ε_p. In this case, it is 5.1×10^{-4} m/s. As mentioned previously, the microchannel was fabricated by milling method. Thus, the inner walls were not as smooth as the polished interface of PMMA due to the milling process. In order to ensure formation of slug flow, 0.35 wt % sodium dodecyl sulfate (SDS) was added to liquid–solid mixture. The surface tension of gas-0.35% SDS solution of liquid–solid mixture is 0.036 N/m. In addition, the fluid and particles properties are summarized in Tables 2 and 3, respectively. It should be noted that the particles were dispersed in deionized water with holdup (ε_p) of 0.3%, and the experiments were conducted at room temperature and atmospheric pressure. The contact angle of the inner wall is hardly to measure and differs with the one of the polished PMMA surface due to difference of roughness. Thus, θ in simulations was represented by the contact angle of air-0.35% SDS solution and liquid–solid mixture-milling surface, as shown in Figure 6. Contact angle θ was measured by a contact angel meter (OCA20, Dataphysics Co., Germany), and the value was $40^\circ \pm 10^\circ$.

Simulation and experimental results corresponding to the process of a gas slug formation were compared, which can be seen in Figure 7 and Table 4. It should be noted that the simulation time (t_s) corresponding to Figures 7 b1, b2, b3 and b4 are 8.3×10^{-3} s, 9.3×10^{-3} s, 10.3×10^{-3} s and 11.3×10^{-3} s, respectively. From Figure 7 and Table 4, it can be seen that the experimental and simulation results show reasonable agreement. However, compared with experimental results, the gas slug tail loses its sphericity in Figures 7b and c. One reason is due to the difference between the set value and true value of the contact angle of the inner wall. Based on the effect of θ on slug flow pattern (will be shown in Figure 10), it can be supposed that the set value is higher than the true value. Another reason is due to the calculation of the curvature at the slug interface with VOF method. As can be seen in Eqs. 6 and 7, the physical properties (ρ and μ) were averaged by the volume fraction. However, the volume fraction (α) is a step function, and the physical properties are not smooth across the interface. Meanwhile, with VOF method, the surface tension was implemented as a body force using the CSF model (Eq. 8). The density which is unsmooth in cells across the interface

Table 2. Fluid Properties in Experiments and Simulations

	ρ, kg/m^3	μ, Pa·s
Air	1.225	1.79×10^{-5}
Liquid-solid suspension	998.2	1.003×10^{-3}

Table 3. Physical Properties of Solid Particles

Materials	Particle diameter (d_p), 10^{-6}m	Density (ρ_p), kg/m^3	Sphericity, φ
Polystyrene	7.928±0.049	1050	≥0.99

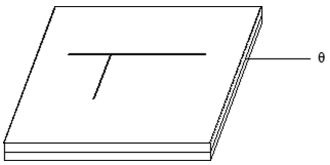

Figure 6. The location of θ measured in experiments.

to calculate the surface tension source term in Eq. 8 will skew this force toward the higher density region.[74] The unsmooth density will lead to the deflection of surface tension, particularly when there exists a big density difference between two phases. As well-known, the interface is tangential to the direction of surface tension. In this case, the density difference is about equal to 1,000 kg/m^3 (ρ_{water}-ρ_{air}). Hence, the gas slug tail in simulations is flatter than that in experiments.

Flow patterns at different operation conditions and wettability of inner walls

As well-known, flow patterns will change with operation conditions. In this article, both v_{l+s} and v_g ranged from 0.17 to 0.85 m/s, Three different flow patterns were obtained, bubbly, transition and slug flows. Figure 8 shows the simulation results of gas-liquid–solid flow pattern map at different operation conditions ($\varepsilon_p = 0.3\%$, $\sigma = 0.0728$N/m, and $\theta = 0^\circ$). It should be noted that for transition flow, the gas slug almost blocks the whole channel too; however, the slug head is obviously narrower than the slug tail, which differs from slug flow. As can be seen in Figure 8, bubble flow transits into slug flow from the top left corner to the bottom right corner of the flow pattern map. Xie[59] experimentally investigated the transition of gas-liquid flow patterns in microchannels with $d_h = 5.09 \times 10^{-4}$ m and $\varepsilon_p = 0.2\%$ (CuO particle, $d_p = 7.016 \times 10^{-6}$ m), it was found that the range of bubble and transition flows was wider in liquid–solid mixture than that in liquid. From Figure 8, it can be seen that both the areas of bubble and slug flows further expands compared with Xie's work. One reason is that the ε_p in simulations is higher than that in Xie's work.[59] It should be noted that for bubbly and transition flows, the entrance length of liquid inlet was elongated to ensure fully developed flow based on Eq.16.

As can be seen in Figure 8, slug flow occupies the major area of the flow pattern map in microscale systems. However, in macrosystems, studies about gas-liquid–solid flow were mainly focused on bubbly regime, and slugging regime was very narrow and usually tried to be avoided in macro fluidization system due to its low stability.[80] Thus, the flow rules of macroscale systems cannot be extended to microscale systems.

Microchannels can be made of materials with different wettability. Flows in microchannels with different materials of wettability were simulated. The variation range of θ is

Table 4. Comparisons of Data between Experiments and Simulations ($v_g = 0.85$m/s, $v_{l+s} = 0.17$m/s, $\sigma = 0.036$N/m, $\varepsilon_p = 0.3\%$ and $\theta = 0^\circ$)

	Experiments	simulations	relative error
L_G, 10^{-3}m	3.70	4.05	9.46%
t_d, 10^{-3}s	3.167	3.445	8.78%

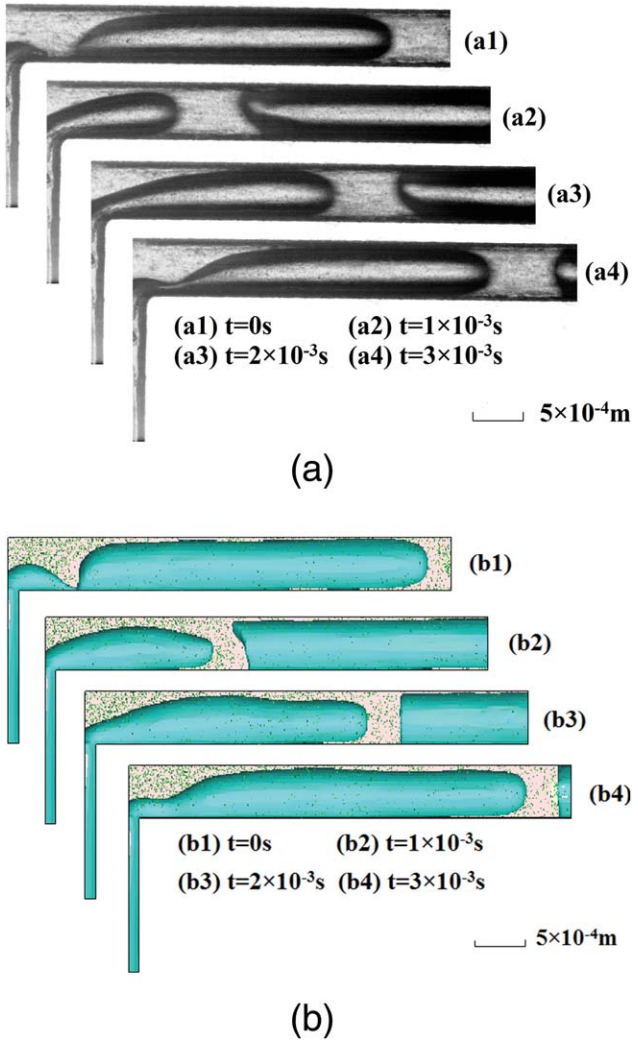

Figure 7. Comparisons between experimental and simulation results ($v_g = 0.85$ m/s, $v_{l+s} = 0.17$ m/s, $\sigma = 0.036$N/m, $\varepsilon_p = 0.3\%$ and $\theta = 0^\circ$).

(a) Experiments, and (b) simulations. [Color figure can be viewed in the online issue, which is available at wileyonlinelibrary.com]

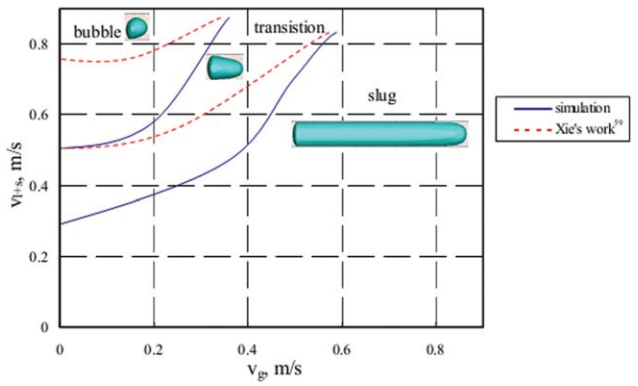

Figure 8. Simulation results of gas-liquid–solid flow pattern map at different operation conditions in microchannels ($\varepsilon_p = 0.3\%$, $\sigma = 0.0728$N/m and $\theta = 0^\circ$).

[Color figure can be viewed in the online issue, which is available at wileyonlinelibrary.com]

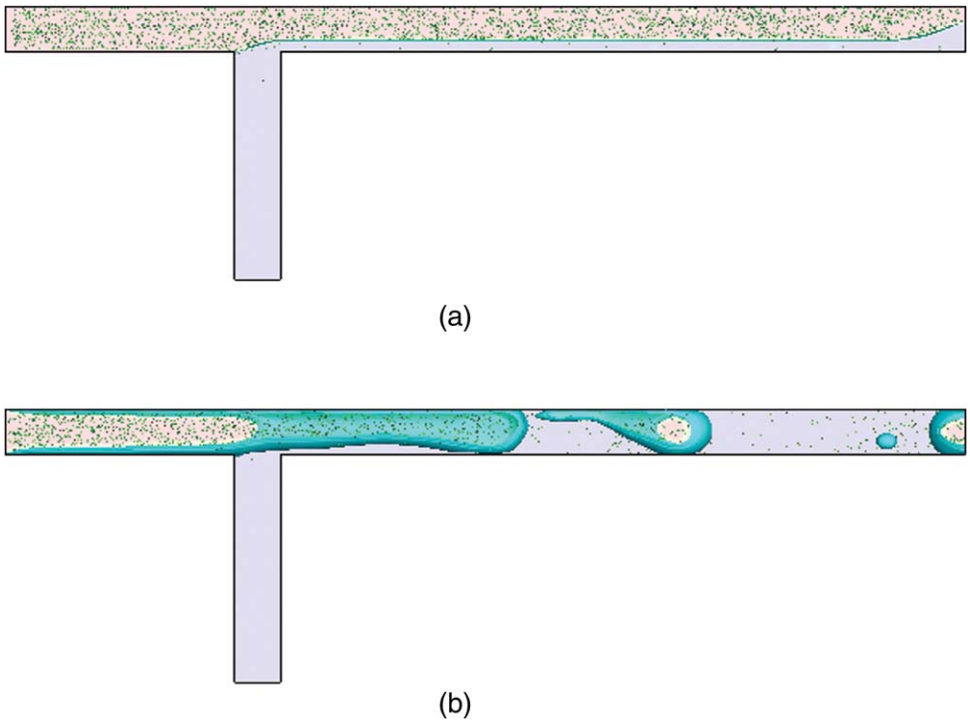

Figure 9. Stratified flow and liquid drop flow ($v_g = 0.85$ m/s, $v_{l+s} = 0.17$ m/s, $\sigma = 0.0728$N/m and $\varepsilon_p = 0.3\%$).

(a) stratified flow ($\theta = 77°$); (b) liquid drop flow ($\theta = 160°$). [Color figure can be viewed in the online issue, which is available at wileyonlinelibrary.com]

0–160°. Simulation results of flow regimes are shown in Table 5.

Transition of flow patterns is found with variation of contact angle. Slug flow transforms into stratified flow when contact angle reaches to 77°, as shown in Figure 9a. If the inner wall is very hydrophobic ($\theta = 160°$), the liquid cannot spread out on the inner wall, and the gas phase turns into continuous phase and liquid exists in the form of liquid drops, as shown in Figure 9b.

Slug flow was observed in cases that $\theta = 0°$, 10°, 30 and 50°. However, the gas slug length and the detachment time are different, as can be seen in Figure 10. The gas slug length first decreases and then increases with the increase of θ. This phenomenon is consistent with Qian and Lawal's[15] 2-D simulation and could be explained as follows. The film which exists between the gas phase and the inner wall thins if the inner wall becomes less hydrophilic. Thus, the resistance effect of the bubble head exerting on liquid phase becomes stronger, which will result in a larger Laplace pressure difference across the bubble interface and a shorter slug formation process. However, when the inner wall becomes further less hydrophilic, it will be favor promoting the breakage of phases into bubbles or drops,[4] which will lead to elongate the gas slug formation process and generate gas slugs of larger length.

As mentioned previously, the wettability of the inner walls will exert a great influence on the flow patterns in microscale systems. However, in macroscale systems, the wall wettability is not a critical factor on flow regimes because bubbly flow is the common flow pattern in macroscale systems and bubbles are scarcely impacted by the inner walls. Only the wettability of the nozzle wall influences the bubble behaviors obviously. Gerlach et al.[75] investigated the influence of the contact angle of the nozzle wall on bubble behaviors, and it was found that the flow pattern kept bubbly flow when the contact angle changed from 0 to 110°.

Table 5. Flow Patterns at Different Values of Contact Angle θ of Microchannel Materials ($v_g = 0.85$m/s, $v_{l+s} = 0.17$m/s, $\sigma = 0.0728$N/m, and $\varepsilon_p = 0.3\%$)

θ, °	Flow patterns
0	slug
10	slug
30	slug
50	slug
77	stratified
120	stratified
160	liquid drop

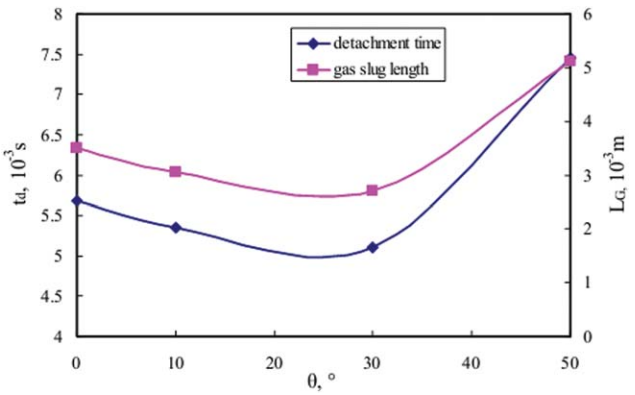

Figure 10. Effect of θ on slug flow ($v_g = 0.85$ m/s, $v_{l+s} = 0.17$ m/s, $\sigma = 0.0728$N/m and $\varepsilon_p = 0.3\%$).

[Color figure can be viewed in the online issue, which is available at wileyonlinelibrary.com]

Table 6. Data Comparisons between Slug Flow in Liquid and in Liquid-Solid Suspensions ($v_g = 0.85$m/s, $v_{l+s} = 0.17$m/s, $\sigma = 0.0728$N/m, $\varepsilon_p = 0.3\%$ and $\theta = 0^\circ$)

	Pure liquid	Particulate suspensions
t_d, 10^{-3}s	5.875	5.710
L_G, 10^{-3}m	4.053	3.556

Effects of particles on gas slug behaviors

As can be seen in Figure 8, slug flow featuring periodicity occupies the majority area of flow-regime map and it is the most important one of flow patterns. The effects of particles on slug flow behaviors are numerically investigated.

First, the difference between two-phase flow and three-phase flow was compared, as shown in Table 6. v_g and v_{l+s} were 0.85 m/s and 0.17 m/s, respectively. ε_p in the liquid–solid mixture was 0.3%.

From Table 6, it can be seen that the slug length in pure liquid is longer than that in liquid–solid mixture. Meanwhile, the detachment time of slug bubble in pure liquid is shorter than that in liquid–solid mixture. The change of liquid properties due to the existence of solid particles leads to the data difference. In the presence of solid particles, it can be supposed that particles change only homogeneous properties, such as viscosity.[81,82] The viscosity of the solid–liquid mixture shows a climbing trend compared with pure liquid. Qian and Lawal[15] investigated the influence of liquid viscosity on Taylor flow in microchannels, and it was found that the slug length decreased with the incensement of liquid viscosity in a microchannel with a 0.5 mm inner diameter. In essence, the dimensionless capillary number ($Ca = \frac{u_c \mu_c}{\sigma}$, where μ_c is the viscosity of continuous phase, and u_c is the velocity of continuous phase), which represents the relative significance between viscous force and surface tension, was usually employed to describe the mechanism of bubble formation in T-junction microchannels. It was found that the formation mechanism transformed from squeezing (slug flow) to transition, and then to dripping (bubbly flow) with the increase of the value of Ca.[83,84] From the definition of Ca, it can be seen its value is proportional to viscosity. However, the existence of particles will increase the superficial viscosity of the liquid. The volume of gas slug is usually bigger than that of the bubble in the same microchannel. Thus, when particles are added to the liquid, the formation mechanism will transform gradually from squeezing toward dripping. That is, both the detachment time and length of gas slug will decrease.

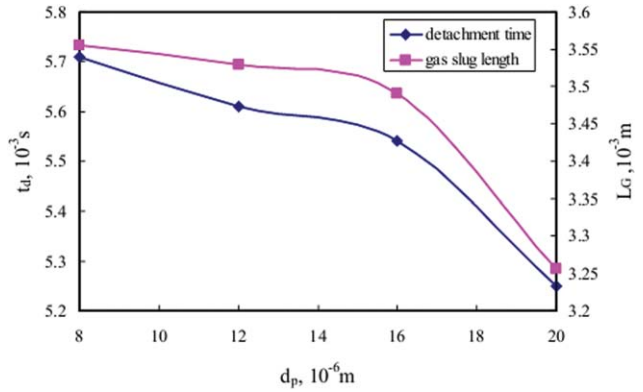

Figure 12. Effect of particle diameter on t_d and L_G ($v_g = 0.85$ m/s, $v_{l+s} = 0.17$ m/s, $\sigma = 0.0728$N/m and $\theta = 0^\circ$).

[Color figure can be viewed in the online issue, which is available at wileyonlinelibrary.com]

Based on the definition that $Ca = \frac{u_c \mu_c}{\sigma}$, the value of Ca in pure liquid is equal to 2.33×10^{-3}. Hence, the mechanism of bubble formation is squeezing ($10^{-4} < Ca < 5.8 \times 10^{-3}$, squeezing regime[83]). Thus, the dominant factor in the process of bubble generation is the Laplace pressure difference across the interface, as shown in the schematic of Figure 11.[24,83] The Laplace pressure is defined as the follows

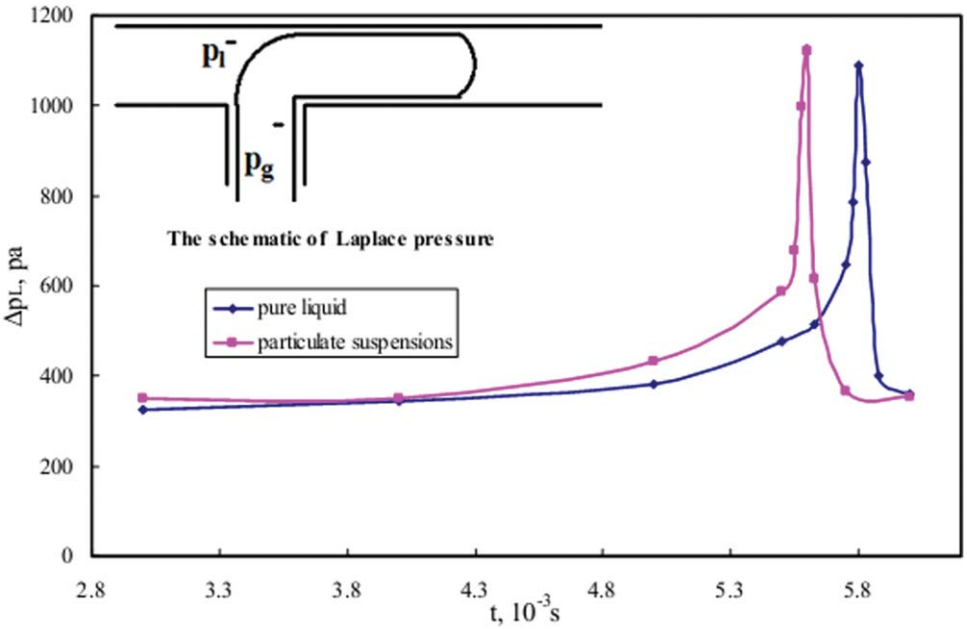

Figure 11. The evolution of Laplace pressure difference inside and outside slug interface ($v_g = 0.85$ m/s, $v_{l+s} = 0.17$ m/s, $\sigma = 0.0728$N/m, $\varepsilon_p = 0.3\%$ and $\theta = 0^\circ$).

[Color figure can be viewed in the online issue, which is available at wileyonlinelibrary.com]

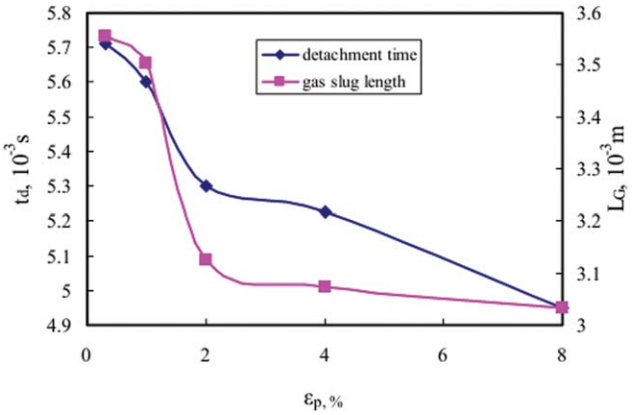

Figure 13. Effect of solid holdup on t_d and L_G ($v_g = 0.85$ m/s, $v_{l+s} = 0.17$ m/s, $\sigma = 0.0728$N/m and $\theta = 0°$).

[Color figure can be viewed in the online issue, which is available at wileyonlinelibrary.com]

$$\Delta P_L = \frac{2\sigma}{r} \tag{20}$$

where r is the local radius of curvature at the bubble interface.

In the schematic of Figure 11 p_l is the pressure in the liquid phase, and p_g is the pressure in the gas phase. The difference between them (p_g-p_l) was employed to estimate the Laplace pressure difference (Δp_L) across the slug interface. It should be noted that the plane shown in the schematic of Figure 11 is the axial surface of the computational domain. Figure 11 shows the evolution of the Δp_L across slug interface. When a slug blocks the main channel, it begins to elongate and grows downstream. The neck of the bubble thins and Δp_L increases. The peak of the pressure difference curve represents the detachment of the slug. When one slug detaches, the following slug commences generation.

Furthermore, it can be seen that pressure difference curve of slug flow in liquid–solid mixture shows a distinction with the one in pure liquid. The peak of the square curve appears earlier than that of the rhombic curve, which represents that the gas slug generation period in liquid–solid mixture is shorter than the one in pure liquid.

Slug flow in gas-liquid–solid system with various values of particle diameter (d_p) were simulated. It should be noted that the total number of particles was kept the same. It is found that both t_d and L_G first decrease slightly, and this downtrend is more obvious with the increase of d_p, which can be seen in Figure 12. There is only a 0.17×10^{-3} s decrement of t_d when d_p increases to 16×10^{-6} m from 8×10^{-6} m. However, when d_p further increases to 20×10^{-6} m from 16×10^{-6} m, the decrement of t_d reaches 0.29×10^{-3} s ($t_d = 5.71 \times 10^{-3}$ s, $d_p = 8 \times 10^{-6}$ m; $t_d = 5.61 \times 10^{-3}$ s, $d_p = 12 \times 10^{-6}$ m; $t_d = 5.54 \times 10^{-3}$ s, $d_p = 16 \times 10^{-6}$ m; $t_d = 5.25 \times 10^{-3}$ s, $d_p = 20 \times 10^{-6}$ m). Besides, the decrement of L_G is only 6.5×10^{-5} m when d_p increases to 16×10^{-6} m from 8×10^{-6} m, and this decrement grows drastically to 0.235×10^{-3} m when d_p further increases to 20×10^{-6} m ($L_G = 3.556 \times 10^{-3}$ m, $d_p = 8 \times 10^{-6}$ m; $L_G = 3.53 \times 10^{-3}$ m, $d_p = 12 \times 10^{-6}$ m; $L_G = 3.491 \times 10^{-3}$ m, $d_p = 16 \times 10^{-6}$ m; $L_G = 3.26 \times 10^{-3}$ m, $d_p = 20 \times 10^{-6}$ m).

Effects of the solid holdup (ε_p) were also investigated. ε_p ranged from 0.3 to 8%, and d_p was kept as 8×10^{-6} m. Figure 13 shows the simulation results and the variation rule of t_d and L_G with ε_P. Similarly, both t_d and L_G decrease with ε_p. Quantificationally, t_d corresponding to the solid holdups of 0.3%, 1%, 2%, 4 and 8% are 5.71×10^{-3} s, 5.6×10^{-3} s, 5.3×10^{-3} s, 5.225×10^{-3} s, and 4.95×10^{-3} s, respectively. Meanwhile, L_G corresponding to these different solid holdups are 3.556×10^{-3} m, 3.504×10^{-3} m, 3.125×10^{-3} m, 3.073×10^{-3} m and 3.033×10^{-3} m, respectively. As known, ε_p is proportional to the cube of d_p, thus, this down trend seems not to be stronger when ε_p gets higher, compared with that when d_p becomes larger.

In fact, the increase of d_p will also leads to the increase of ε_p if the total number of particles is kept the same. As mentioned previously, particles would change the homogeneous properties of liquid–solid mixture, such as viscosity. Tsuchiya et al.[81] presented a correlation to forecast the effective viscosity of liquid–solid mixture as follows

$$\frac{\mu_s}{\mu_l} = \exp\left[\frac{K\varepsilon_p}{1-(\varepsilon_p/\varepsilon_{pc})}\right] \tag{21}$$

$$K = \frac{3.1 - 1.4\tanh\left[0.3-(100u_t)\right]}{\phi} \tag{22}$$

$$\varepsilon_{pc} = \{1.3 - 0.1\tanh\left[0.5(10-100u_t)\right]\}\varepsilon_{p0} \tag{23}$$

where μ_s is the effective viscosity of the liquid–solid mixture, ϕ is the particle sphericity, u_t is the particle terminal velocity in liquid phase, ε_{pc} is the critical solid holdup, and ε_{p0} is the solid holdup at the incipient fluidization state. From Eqs. 21–23, it can be found that μ_s is always higher than μ_l, and increases exponentially with ε_p, i.e., the effects of solid holdup on the effective viscosity becomes stronger with the increase of ε_p. Based on Eqs. 21–23, and the definition that $Ca = \frac{u_c \mu_c}{\sigma}$, Ca ranges from 2.33×10^{-3} to 2.92×10^{-3} ($0 \le \varepsilon_p \le 8\%$). The mechanism of bubble formation still locates in squeezing regime when $\varepsilon_p = 8\%$.[83] However, as mentioned previously, the increase of superficial viscosity will move the mechanism of bubble formation toward dripping regime, which leads to the decrease of both t_d and L_G.

Particles' behaviors of slug flow in gas-liquid–solid system at microscale

The particle distribution along the axial direction during the formation of a gas slug was investigated. This process can be divided by four stages, as can be seen in the snapshots of Figure 14 (a) the gas slug enters the main channel, (b) the slug blocks almost the whole cross section of the main channel, (c) the slug elongates downstream direction and the neck thins, and (d) the neck breaks and the following slug begins to generate. In order to make the snapshots more compact, the inlet zones of liquid–solid suspensions were not shown in the snapshots. The mixing domain was divided into 10 segments uniformly along the axial direction, as shown in the snapshot (d) in Figure 14. The number of solid particles (N_p) in each segment was counted. From the analysis of the snapshots and the curves in Figure 14, it can be seen that particles mainly concentrate in liquid area between two adjacent gas slugs and transport downstream with liquid slugs. For the curve of 28.25×10^{-3} s (•) in Figure 14, two peaks appear in segments 1 and 7, respectively. Liquid occupies majority part of the two segments.

Meanwhile, particles distributions along radial direction in both gas and liquid slugs were investigated. Two segments

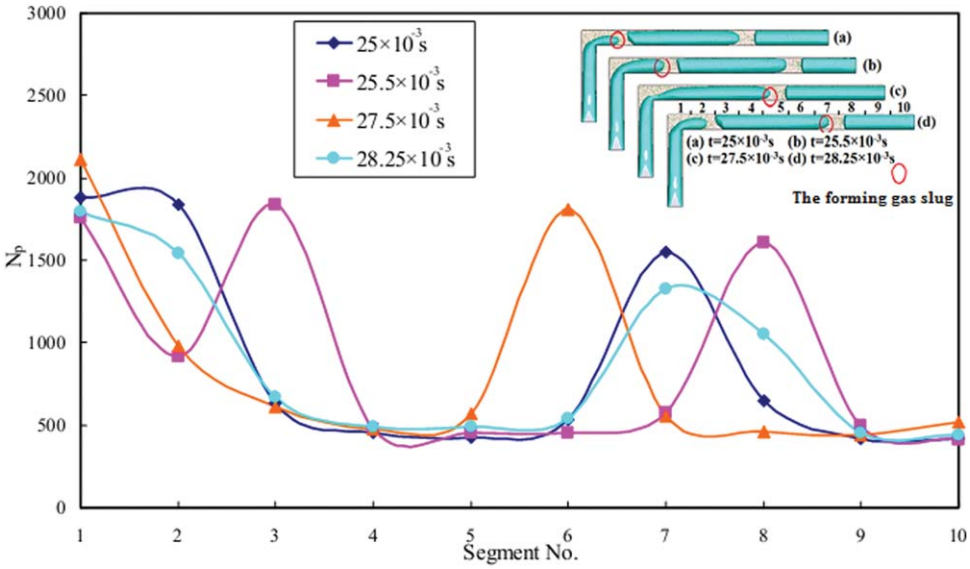

Figure 14. Particles distribution along axial direction during the formation of a gas slug ($v_g = 0.85$ m/s, $v_{l+s} = 0.17$ m/s, $\sigma = 0.0728$N/m, $\varepsilon_p = 0.3\%$ and $\theta = 0°$).

[Color figure can be viewed in the online issue, which is available at wileyonlinelibrary.com]

of length corresponding to the gas and liquid slugs (at $t = 25.5 \times 10^{-3}$ s) were employed as samples to analyze particles distribution along radial direction. The segments were divided into 10 parts uniformly along radial direction as shown in the schematic of Figure 15. In the same way, N_p in each part was counted. Figure 15 shows the simulation results of particles distribution along radial direction in gas and liquid slugs. The curve with symbol of solid lozenge represents liquid slug and the solid square one represents gas slug. For gas slug, two peaks appear at the two walls. In fact, solid particles are mainly distributed in the liquid films between the gas slug and the inner wall. The area of the liquid film becomes smaller from the wall to the center of the channel along radial direction. Hence, the numbers of particles in parts 1 and 10 are much larger than the values in other parts.

Compared with Eulerian multiphase model, DPM method holds its advantage to track the trajectory of each particle. A particle whose residence time is corresponding to the strongest peak in Figure 17 was tracked, and its trajectory near the T-junction is shown in Figure 16. It should be noted other particles are not in shown in these snapshots of Figure 16. The interval between each snapshot in Figure 16 is 0.75×10^{-3} s. As can be seen clearly in Figure 16, the particle is blocked by the formed gas slug and moves downstream very slowly (Figures 16 a–d). Once the gas slug detaches, this particle enters the liquid slug (Figure 16e), and transports downstream quickly with the liquid slug (Figures 16f–g).

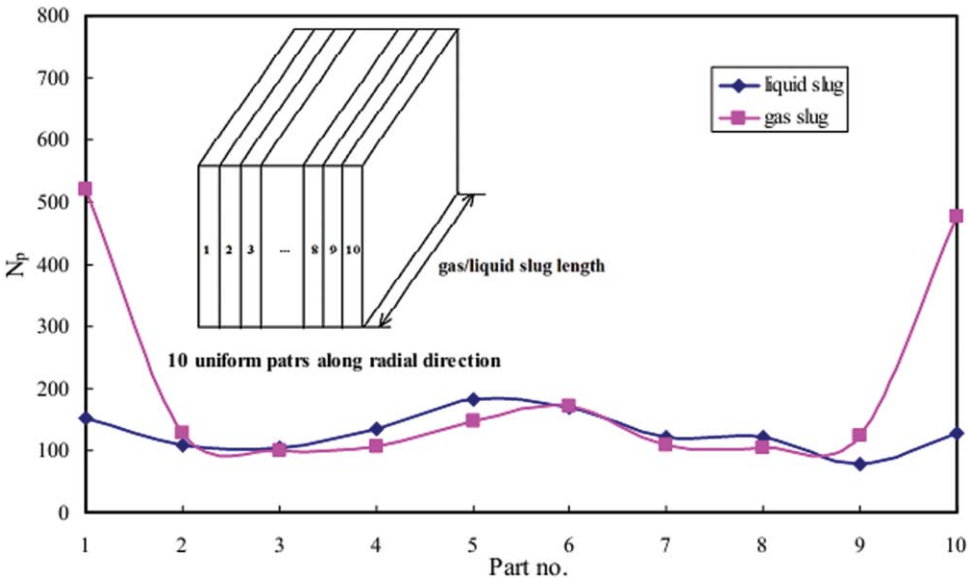

Figure 15. Particles distribution along radial direction in liquid or gas slug at $t = 25.5 \times 10^{-3}$ s ($v_g = 0.85$ m/s, $v_{l+s} = 0.17$ m/s, $\sigma = 0.0728$N/m, $\varepsilon_p = 0.3\%$ and $\theta = 0°$).

[Color figure can be viewed in the online issue, which is available at wileyonlinelibrary.com]

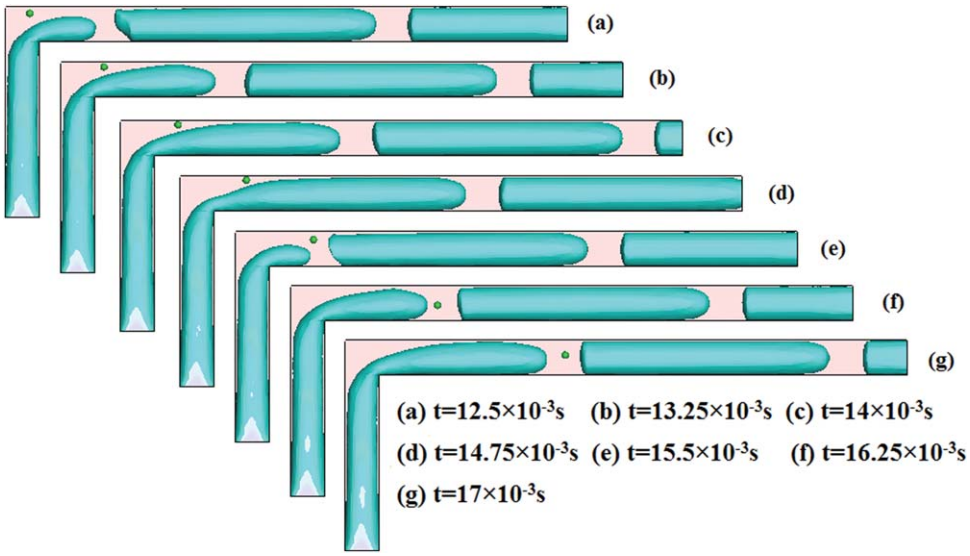

Figure 16. A particle's trajectory near the T-junction ($v_g = 0.85$ m/s, $v_{l+s} = 0.17$ m/s, $\sigma = 0.0728$N/m, $\varepsilon_p = 0.3\%$ and $\theta = 0^\circ$).

[Color figure can be viewed in the online issue, which is available at wileyonlinelibrary.com]

Besides, it can be inferred that the velocity of this particle in the mixing zone is much bigger than that in the inlet zone of liquid–solid suspensions. Because in the inlet zone of liquid–solid suspensions, particles move to the T-junction at the speed of about v_{l+s}. However, in the mixing zone, particles transport downstream with liquid slug. The velocity of the liquid slug is about equal to the sum of v_g and v_{l+s}, and is much bigger than v_{l+s}.

Mixing behaviors of gas-liquid–solid flow in microchannels

The dimensionless variance of residence time (σ_θ^2) is the classic parameter to describe the backmixing degree. It is defined as follows

$$\sigma_\theta^2 = \frac{\sigma_t^2}{\bar{t}^2} \tag{24}$$

$$\bar{t} = \int_0^\infty tE(t)dt \tag{25}$$

$$\sigma_t^2 = \int_0^\infty t^2 E(t)dt - \bar{t}^2 \tag{26}$$

The value of σ_θ^2 ranges from 0 to 1. σ_θ^2 of plug flow reactor (PFR) is 0, meaning that backmixing does not exist. σ_θ^2 of continuous stirred-tank reactor (CSTR) is 1, indicating that backmixing degree attains its maximum. Generally, the degree of mixing becomes weaker with the decrement of σ_θ^2.

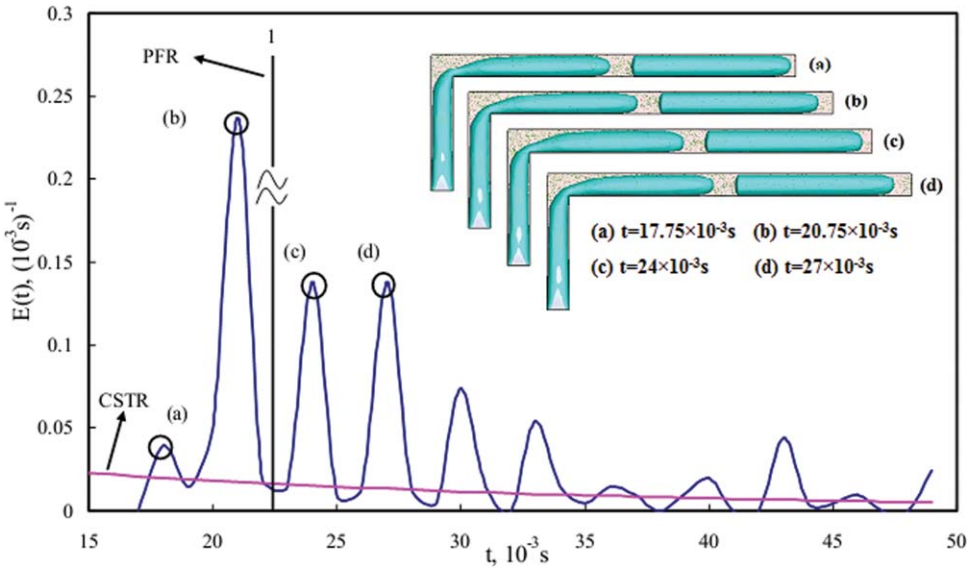

Figure 17. Simulation results of RTD of particles and liquid phase in slug flow ($v_g = 0.85$ m/s, $v_{l+s} = 0.17$ m/s, $\sigma = 0.0728$N/m, $\varepsilon_p = 0.3\%$ and $\theta = 0^\circ$).

[Color figure can be viewed in the online issue, which is available at wileyonlinelibrary.com]

Table 7. σ_θ^2 and $\bar{t}$ of Particles and Liquid Phase in Different Flow Patterns ($v_g = 0.85$m/s, $v_{l+s} = 0.17$m/s, $\sigma = 0.0728$N/m and $\varepsilon_p = 0.3\%$)

	Slug	liquid drop	stratified
σ_θ^2	0.145	0.053	—
$\bar{t}$,10^{-3}s	24.99	29.82	—

Table 7 shows $\bar{t}$ and σ_θ^2 of particles in different flow patterns. The integral value in Eqs. 24–26 was calculated by variable step-size compound Simpson formula. In fact, the impulse is exactly the group of particles injected at the 100th time step (5×10^{-4} s). To facilitate the narrative, this group of particles is named as "injection-1". In slug and liquid drop flows, about 10% of the particles contained in "injection-1" still resides in the microchannel at $t = 50$ ms (10,000 time steps). If this part of particles are considered, the trail of RTD curve will be very long and the accuracy of the numerical integral in Eqs. 24–26 will be influenced seriously. Therefore, this part of particles were treated as ineffective ones and ignored. Unfortunately, in stratified flow, more than a third of particles contained in "injection-1" still resides in the microchannel. Hence, $\bar{t}$ and σ_θ^2 of particles in stratified flow were not obtained. Cisne et al.[47] gave the definition of Stokes number (St)

$$St = \frac{\rho_p {d_p}^2 u_p}{18 u_{l+s} D} \tag{27}$$

where D is the characteristic dimension of the microchannel. St shows the ratio t_R/t_F, between the time of response of the particle to the action of the fluid $t_R = \frac{\rho_p {d_p}^2}{18\mu}$, and the characteristic flow time $t_F = u_p/D$. When St limits to 0, particles respond quickly to flow changes, and behave as "tracers", following the streamlines of the flow. The critical value of St number is 0.18, i.e., if the St number is smaller than 0.18, particles behave as tracers. In this case, the St is of the order of O (10^{-3}). Thus, the mixing behaviors of particles can also represent the RTD of liquid phase. Analyses in more details were done as follows. Table 7 shows the dimensionless variance of residence time and average residence time of particles and liquid phase in different flow patterns. Detailed analysis of mixing behaviors is as follows.

Figure 17 shows the RTD of particles and liquid phase obtained from the simulation results. However, the RTD curve is similar to a damping vibration curve, as shown in Figure 17. As mentioned in the analysis of particles distribution along axial direction, particles mainly concentrate in liquid slug. Therefore, particles are separated into different major parts by gas slug. One part will transport downstream, the other parts will be blocked in the T-junction area and transport downstream with the following liquid slug, which leads to the difference of residence time. The flow snapshots corresponding to the first four peaks are also shown in Figure 17. It is found that a liquid slug is exiting the computational domain in each snapshot, and the interval between each impulse just equals to the period of a gas slug formation process. The flow characteristics of particles show a periodic rule in both temporal and spatial scales, which are dominated by the gas slug length and the formation time of a gas slug.

Figure 18 shows RTD of particles and liquid phase in liquid drop flow. Similarly to the RTD curve of slug flow, the RTD curve of liquid drop flow consists of different peaks. With the same method, the flow snapshots corresponding to the first four impulses in the RTD curve are shown in Figure 18. It is also found that a liquid drop is exiting the computational domain in each snapshot, the gas inlet zones were not shown in order to make snapshots more compact. From this phenomenon, it can be inferred that particles mainly distribute in liquid drops. However, compared with RTD curve, three difference points should be pointed out. First, the impulses are not as strong as slug flow. It can be explained as follows. In liquid drop flow, liquid turns into discontinuous phase and will be squeezed into drops by gas phase. During the squeezing process, a few particles will penetrate into gas phase, as can be seen in Figure 18. Second, from Table 7, it is found that $\sigma^2_{\theta,slug} > \sigma^2_{\theta,liquiddrop}$. That is, the backmixing degree of liquid drop flow is weaker than that of slug flow. It is for that the gas phase turns into continuous phase in liquid drop flow, and the blocking effect of gas slug

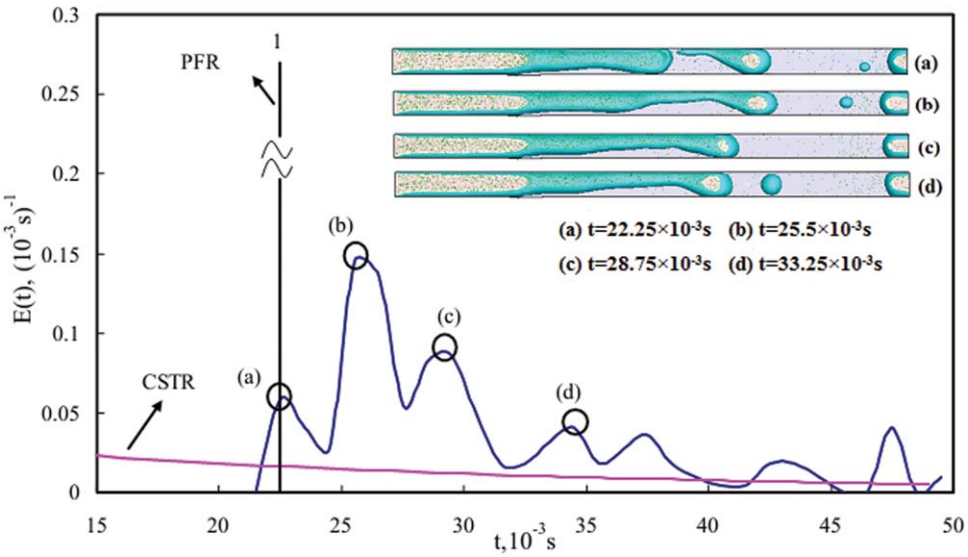

Figure 18. RTD curve of particles and liquid phase in liquid drop flow ($v_g = 0.85$ m/s, $v_{l+s} = 0.17$ m/s, $\sigma = 0.0728$N/m, $\varepsilon_p = 0.3\%$ and $\theta = 160°$).

[Color figure can be viewed in the online issue, which is available at wileyonlinelibrary.com]

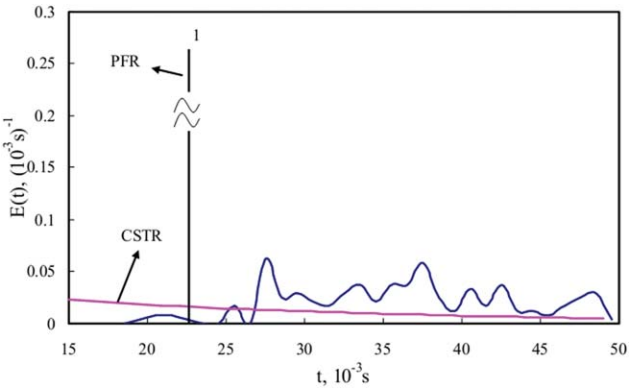

Figure 19. RTD curve of particles and liquid phase in stratified flow. ($v_g = 0.85$ m/s, $v_{l+s} = 0.17$ m/s, $\sigma = 0.0728$N/m, $\varepsilon_p = 0.3\%$ and $\theta = 77°$).

[Color figure can be viewed in the online issue, which is available at wileyonlinelibrary.com]

Table 8. σ_θ^2 and $\bar{t}$ of Gas Phase in Different Flow Patterns ($v_g = 0.85$m/s, $v_{l+s} = 0.17$m/s, $\sigma = 0.0728$N/m and $\varepsilon_p = 0.3\%$).

	Slug	liquid drop	stratified
σ_θ^2	0.062	0.184	0.303
$\bar{t}$,10^{-3}s	12.197	16.595	17.054

does not exist. Third, $\bar{t}_{slug} < \bar{t}_{liquiddrop}$, which can be reasoned as follows, once a liquid slug or drop is formed, its velocity is approximately equal to the sum of v_{l+S} and v_g, thus, it is much higher than v_{l+s}. In liquid drop flow, the area where a liquid drop is formed located in the downstream of the location where a liquid slug is formed in slug flow. Hence, particles reside in the computational domain longer compared with slug flow.

Figure 19 shows the particles RTD curve of stratified flow. Compared with slug flow and liquid drop flow, no obvious impulse exists on the curve. In stratified flow, no liquid drop or slug is formed and particles mainly distribute in the upper liquid, which can be seen in Figure 9a. Although $\bar{t}$ and σ_θ^2 of particles and liquid in stratified flow were not obtained, it can be inferred that the backmixing is more serious compared with the other two flow patterns, which can be attributed to that liquid phase cannot be separated by gas phase. Meanwhile, as can be expected, $\bar{t}$ is much bigger than that of slug and liquid drop flow. The reason is that velocity of the upper liquid is smaller than that of liquid drop or slug.

For a macro gas-liquid–solid circulating fluidized bed, there existed generally only one peak on the liquid phase RTD curve,[85] differing from any one mentioned previously. In bubbly regime at macroscale, the ratio of bubble diameter to bed or column diameter is far smaller than that at microscale, and gas phase will not exert any blocking or squeezing effect on liquid phase. Hence, RTD curve with two or more peaks does not appear in bubbly regime at macroscale. In addition, σ_θ^2 of liquid phase in the macro gas-liquid–solid circulating fluidized bed (including the riser and the downer) ranged from 0.1 to 0.4.[85] Basically, the liquid backmixing of liquid drop flow and slug flow weakens compared with bubbly flow at macroscale.

The RTD of gas phase in the three different flow patterns were compared. The viscosity of gas is far smaller than that of liquid phase. Thus, based on Eq. 27, solid particles with d_p of 1×10^{-6} m) are employed as tracers during simulations. As can be seen in Figure 20 and Table 8, backmixing degree of gas phase in liquid drop flow and stratified flow is more evident compared to slug flow. Because in slug flow, the gas phase is the discontinuous phase, the separation of gas slugs by the liquid slugs reduces axial gas mixing.[17,23] Only in slug flow, gas phase exists in the form of discontinuous phase and occupies the whole cross section of the microchannel. Thus, the velocity of gas slug equals about to $v_g + v_{l+s}$. Therefore, the average residence time of slug flow is smaller compared with liquid drop and stratified flows.

Furthermore, the influence of gas-liquid ratio (v_g/v_{l+s}) on mixing behaviors of slug flow was investigated, as shown in Figure 21. This ratio decreased from 5:1 to 1:1 with equal

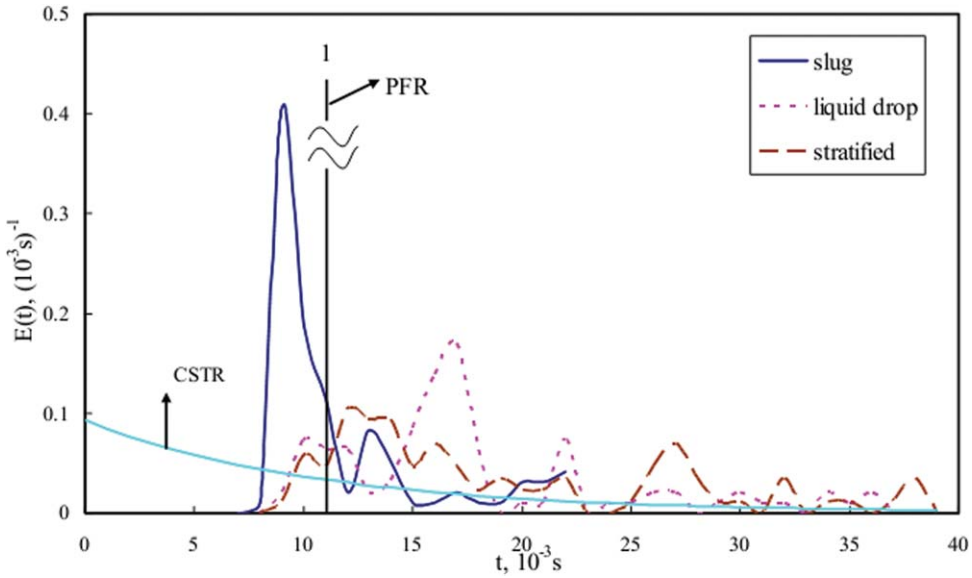

Figure 20. RTD of gas phase in three flow patterns in microchannels ($v_g = 0.85$ m/s, $v_{l+s} = 0.17$ m/s, $\sigma = 0.0728$N/m and $\varepsilon_p = 0.3\%$).

[Color figure can be viewed in the online issue, which is available at wileyonlinelibrary.com]

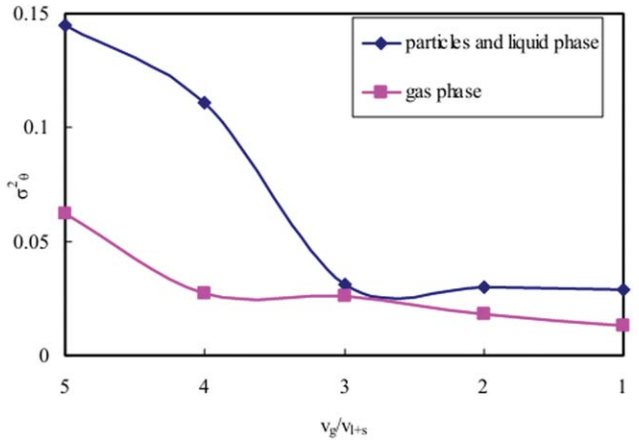

Figure 21. Effect of gas-liquid ratio on backmixing degree in slug flow. ($v_{l+s} = 0.17$ m/s, $\sigma = 0.0728$N/m and $\varepsilon_p = 0.3\%$).

[Color figure can be viewed in the online issue, which is available at wileyonlinelibrary.com]

difference. Specifically, v_{l+s} was kept as 0.17 m/s, and v_g was 0.85 m/s, 0.68 m/s, 0.51 m/s, 0.34 m/s and 0.17 m/s, respectively. From Figure 21, it can be seen that $\sigma^2_{\theta,s \text{ and } l}$ first decreases when v_g/v_{l+s} decreases from 5:1 to 3:1. In other words, the backmxing degree becomes weaker. It can be explained as follows. When the v_g/v_{l+s} decreases, the liquid slug will be elongated and the gas slug will be shortened due to the increase of liquid holdup. Thus, the number of particles in each liquid slug is more, which will lead to the narrowing of RTD curve and the decrease of $\sigma^2_{\theta,s \text{ and } l}$. However, when v_g/v_{l+s} further decreases to 2:1, and then to 1:1, reaches a relative stable value. It is because that when v_g/v_{l+s} decreases to 3:1, the liquid slug is long enough to contain almost all of particles injected at the same time. Therefore, the RTD curve of particles is very close to that of PFR and the value of $\sigma^2_{\theta,s \text{ and } l}$ is close to 0. Hence, $\sigma^2_{\theta,s \text{ and } l}$ does not decrease with the decrement of v_g/v_{l+s} any more. However, the influence of gas liquid ratio on $\sigma^2_{\theta,g}$ is not so strong. $\sigma^2_{\theta,g}$ goes down gradually with the decrease of v_g/v_{l+s}. The particle tracers are included in one gas slug, and the shortening of gas slug will weaken the backmixing of the gas phase.

Concluding Remarks

In this article, flow and mixing characteristics of gas-liquid–solid system in microchannels were first simulated by employing CFD-VOF—DPM method. Experimental and simulation results were compared and reasonable agreements were obtained. Compared with slug flow in pure liquid, both t_d and L_G decrease, which can be attributed to the addition of solid particles. The period length of particles' flow is equal to that of a gas slug formation. By increasing the contact angle of microchannel walls, slug flow (0–50°), stratified flow (77–120°) and liquid drop flow (160°) are obtained successively. RTD curves of solid particles in slug and liquid drop flows are similar to a damping vibration curve due to the existence of segmented liquid slug or drop. Among the three flow patterns, the backmixing of solid and liquid phase reaches its weakest degree in liquid drop flow. RTD of gas phase in slug flow is obviously narrower than stratified and liquid drop flows due to the weak axial back mixing of the gas phase in slug flow. These flow and mixing rules provide a basis for the possible applications in process industries and further study on such microdevices.

The interaction of fluid and wall was simulated by varying the static contact angle. It is equivalent to assume that the gas-liquid–solid wall is always in equilibrium at the inner region of contact line, resulting in the inaccuracy of surface tension at bubble interface. The formulation of nonequilibrium, which corresponds to dynamic contact angle, and the application of slip boundary conditions are the future work. In addition, in order to get more detailed behavior of gas-liquid–solid flow in microchannels, the effects of particles on the local velocity and pressure fields should be analyzed in the future.

Acknowledgments

The authors gratefully acknowledge the support of the high performance computing center (hpcc) of Tianjin University. Authors also acknowledge the assistance in experiments providing by Professor Ma Youguang and Ph.D. candidate Wu Yining of Tianjin University.

Literature Cited

1. Chen G, Yuan Q. Micro-chemical technology. *J Chem Ind Eng*. 2003;54:427–439.
2. Yi M, Bau HH. The kinematics of bend-induced mixing in microconduits. *Int J Heat Fluid Flow*. 2003;24:645–656.
3. Schönfeld F, Hardt S. Simulation of helical flows in microchannels. *AIChE J*. 2004:50:645–656.
4. Shao N, Gavriilidis A, Angel P. Flow regimes for adiabatic gas-liquid flow in microchannels. *Chem Eng Sci*. 2009;64:5749–2761.
5. Santos RM, Kawaji M. Numerical modeling and experimental investigation of gas-liquid slug formation in a microchannel T-junction. *Int J Multiphase Flow*. 2010;36:314–323.
6. Liu H, Vandu CO, Krishna R. Hydrodynamics of taylor flow in vertical capillaries: Flow regimes, bubble rise velocity, liquid slug length, and pressure drop. *Ind Eng Chem Res*. 2005;44:4884–4897.
7. van Stejin V, Kreutzer MT, Klejin CR. Velocity fluctuations of segmented flow in microchannels. *Chem Eng J*. 2008;135:159–165.
8. Zhao TS, Bi QC. Co-current air-water two-phase flow patterns in vertical triangular microchannels. *Int J Multiphase Flow*. 2001;27:765–78.
9. Chung PM-Y, Kawaji M. The effect of channel diameter on adiabatic two- phase flow characteristics in microchannels. *Int J Multiphase Flow*. 2004;30:735–761.
10. Akbar MK, Plummer DA, Ghanaian SM. Gas-liquid two-phase flow regimes in microchannels. ASME Int Mechanical Engineering Congress and Exposition; 2002.
11. Waelchli S, von Rohr PR. Two-phase flow characteristics in gas-liquid microreactors. *Int J Multiphase Flow*. 2006;32:791–806.
12. de Menech M, Garstecki P, Jousse F,Stone HA. Transition from squeezing to dripping in a microfluidic T-shaped junction. *J Fluid Mech*. 2008;595:141–161.
13. Xu JH, Li SW, Tan J, Luo GS. Correlations of droplet formation in T-junction microfluidic devices: from squeezing to dripping. *Microfluid Nanofluid*. 2008;5:711–717.
14. Triplett KA, Ghiaasiaan SM, Abdel-Khalik SI, Sadowski, DL. Gas-liquid two-phase flow in microchannels Part 1: two-phase flow patterns. *Int J Multiphase Flow*. 1999;25:377–394.
15. Qian D, Lawal A. Numerical study on gas and liquid slugs for Taylor flow in a T-junction microchannel. *Chem Eng Sci*. 2006;61:7609–7625.
16. Bretherton FP. The motion of long bubbles in tubes. *J Fluid Mech*. 1961;10:166–188.
17. Gupta R, Fletcher DF, Haynes BS. On the CFD modelling of Taylor flow in microchannels. *Chem Eng Sci*. 2009;64:2941–2950.
18. Asadolahi AN, Gupta R, Fletcher DF, Haynes BS. CFD approaches for the simulation of hydrodynamics and heat transfer in Taylor flow. *Chem Eng Sci*. 2011;66:5575–5584.

19. Kumar V, Vashisth S, Hoarau Y, Nigam KDP. Slug flow in curved microreactors: Hydrodynamic study. *Chem Eng Sci.* 2007;62:7494–7504.
20. Kashid MN, Platte F, Agar DW, Turek S. Computational modelling of slug flow in a capillary microreactor. *J Comput Appl Math.* 2007;203:487–497.
21. Goel D, Buwa VV. Numerical simulations of bubble formation and rise in microchannels. *Ind Eng Chem Res.* 2009;48:8109–8120.
22. Taha T, Cui ZF. Hydrodynamics of slug flow inside capillaries. *Chem Eng Sci.* 2004;59:1181–1190.
23. Taha T, Cui ZF. CFD modelling of slug flow in vertical tubes. *Chem Eng Sci.* 2006;61:676–687.
24. Garstecki, P., Fuerstamn, M.J., Howard A, Stone A, George MW. Formation of droplets and bubbles in a microfluidic T-junction-scaling and mechanism of break-up. *Lab Chip.* 2006;6:437–446.
25. Sobieszuk P, Cygański P, Pohorecki R. Bubble lengths in the gas-liquid Taylor flow in microchannels. *Chem Eng Res Des.* 2010;88:263–269.
26. van Stejin V, Kreutzer MT, Kleijn CR. μ-PIV study of the formation of segmented flow in microfluidic T-junctions. *Chem Eng Sci.* 2007;62:7505–7514.
27. Fu T, Ma Y, Funfschilling D, Zhu C, Li HZ. Breakup dynamics of slender bubbles in non-newtonian fluids in microfluidic flow-focusing devices. *AIChE J.* 2012.doi:10.1002/aic.13723.
28. Roy S, Al-Dahhan M. Flow distribution characteristics of a gas-liquid monolith reactor. *Catal Today.* 2005;105:396–400.
29. Koptyug IV, Ilyina LY, Matveev AV, Sagdeev RZ, Parmon VN, Altobelli SA. Liquid and gas flow and related phenomena in monolithic catalysts studied by 1H NMR micro imaging. *Catal Today.* 2001;69:385–392.
30. Wang K, Lu YC, Tan J, Yang BD, Luo GS. Generating gas/liquid/liquid three-phase microdispersed systems in double T-junctions microfluidic device. *Microfluid Nanofluid.* 2010;8:813–821.
31. Tonkovich AY, Zilka JL, LaMont MJ, Wang Y, Wegeng RS. Microchannel reactors for fuel processing applications. I. Water gas shift reactor. *Chem Eng Sci.* 1999;54:2947–2951.
32. Jähnisch K, Baerns M, Hessel V, Ehrfeld W, Haverkamp V, Löwe H, Wille C, Guber A. Direct fluorination of toluene using elemental fluorine in gas/liquid microreactors. *J Fluorine Chem.* 2000;105:117–128.
33. Abdallah R, Magnico P, Fumey B, de Bellefon C. CFD and kinetic methods for mass transfer determination in a mesh microreactor. *AIChE J.* 2006;52:2230–2237.
34. Yue J, Luo L, Gonthier Y, Chen G, Yuan Q. An experimental study of air-water Taylor flow and mass transfer inside square microchannels. *Chem Eng Sci.* 2009;64:3697–3708.
35. Abiev RS, Lavretsov IV. Hydrodynamics of gas-liquid Taylor flow and liquid–solid mass transfer in mini channels: Theory and experiment. *Chem Eng J.* 2011;176-177:57–64.
36. Gupta R, Fletcher DF, Haynes BS. CFD modelling of flow and heat transfer in the Taylor flow regime. *Chem Eng Sci.* 2010;64:2094–2107.
37. Mehdizadeh A, Sherif SA, Lear WE. Numerical simulation of thermofluid characteristics of two-phase slug flow in microchannels. *Int J Heat Mass Tran.* 2011;54:3457–3465.
38. He Q, Fukagata K, Kasagi N. Numerical simulation of gas-liquid two-phase flow and heat transfer with dry-out in amicro tube. 6th International Conference on Multiphase Flow; 2007.
39. Ding Y, Bi HT, Wilkinson DP. Three-dimensional numerical simulation of water droplet emerging from a gas diffusion layer surface in microchannels. *J Power Sources.* 2010;195:7278–7288.
40. Du W, Zhang L, Bi XT, Wilkinson DP, Stumper J, Wang H. Gas-liquid two-phase flow in minichannels with liquid side introduction. *Ind Eng Chem Res.* 2010;49:6709–6721.
41. Colosqui CE, Cheah MJ, Kevrekidis IG, Benziger JB. Droplet and slug formation in polymer electrolyte membrane fuel cell flow channels: The role of interfacial forces. *J Power Sources.* 2011;196:10057–10068.
42. Nisisako T, Torii T, Higuchi T. Droplet formation in a microchannel network. *Lab Chip.* 2002;2:24–26.
43. Dreyfus R, Tabeling P, Willaime H. Ordered and disordered patterns in two-phase flows in microchannels. *Phys Rev Lett.* 2003;90:144505.
44. Kobayashi I, Mukataka S, Nakajima M. CFD simulation and analysis of emulsion droplet formation from Straight-through microchannels. *Langmuir.* 2004;20:9868–9877.
45. Kobayashi I, Vladisavljević GT, Uemura K, Nakajima M. CFD analysis of microchannel emulsification: Droplet generation process and size effect of asymmetric straight flow-through microchannels. *Chem Eng Sci.* 2011;66:5556–5565.
46. Ookawara S, Street D, Ogawa K. Numerical study on development of particle concentration profiles in a curved microchannel. *Chem Eng Sci.* 2006;61:3714–3724.
47. Cisne RLC Jr, Vasconcelos TF, Parteli EJR, Andrade JS Jr. Particle transport in flow through a ratchet-like channel. *Microfluid Nanofluid.* 2011;10:543–550.
48. Ai Y, Park S, Zhu J, Xuan X, Beskok A, Qian S. DC electrokinetic particle transport in an L-shaped microchannel. *Langmuir.* 2009;26:2937–2944.
49. Khashan SA, Furlani EP. Effects of particle-fluid coupling on particle transport and capture in a magnetophoretic microsystem. *Microfluid. Nanofluid.* 2012;12:565–580.
50. Jensen KF. Microreaction engineering-is small better? *Chem Eng Sci.* 2001;51:293–303.
51. Losey MW, Schmidit MA, Jensen KF. Microfabricated multiphase packed-bed reactors: characterization of mass transfer and reactions. *Ind Eng Chem Res.* 2001;40:2555–2562.
52. Kobayashi J, Mori Y, Okamoto K, Akiyama R, Ueno M, Kitamori T, Kobayashi S. A microfluidic device for conducting gas-liquid–solid hydrogenation reactions. *Science.* 2004;304:1305–1308.
53. Kobayashi J, Mori Y, Kobayashi S. Multiphase organic synthesis in microchannels reactors. *Chem Asian J.* 2006;1-2:22–35.
54. Hessel V, Angeli P, Gavriilidis A, Löwe H. Gas-iquid and gas-liquid–solid microstructured reactors: contacting principles and applications. *Ind Eng Chem Res.* 2005;44:9750–9769.
55. Geyer K, Codee DCJ, Seeberger PH. Microreactors as tools for synthetic chemists-the chemists' round-bottomed flask of the 21st century?. *Chem Eur J.* 2006;12:8434–8442.
56. Luo G, Du L, Wang Y, Lu Y, Xu J. Controllable preparation of particles with microfluidics. *Particuology.* 2011;9:545–558.
57. Wang K, Wang YJ, Chen GG, Luo GS, Wang JD. Enhancement of mixing and mass transfer performance with a microstructure minireactor for controllable preparation of $CaCO_3$. *Ind Eng Chem Res.* 2007;46:6092–6098.
58. Ufer A, Sudhoff D, Mescher A, Agar DW. Suspension catalysis in a liquid-liquid capillary microreacor. *Chem Eng J.* 2011;167:468–474.
59. Xie L. Effects of Fine Particle on the Gas-Liquid Mass Transfer in the Microchannel. Tianjin, *China: Tianjin University;* 2010.
60. Liedtke A-K, Bornette F, Philippe R, de Bellefon C. Gas-liquid–solid ''slurry Taylor'' flow: Experimental evaluation through the catalytic hydrogenation of 3-methyl-1-pentyn-3-ol. *Chem Eng J.* 2012. doi:http://dx.doi.org/10.1016/j.cej.2012.07.100.
61. Li Y, Zhang J, Fan L—S. Numerical simulation of gas-liquid–solid fluidization systems using a combined CFD-VOF—DPM method: bubble wake behavior. *Chem Eng Sci.* 1999;54:5101–5107.
62. Chen C, Fan L—S. Discrete simulation of gas-liquid bubble columns and gas-liquid–solid fluidized beds. *AIChE J.* 2004;50:288–301.
63. van Sint Annaland M, Deen NG, Kuipers JAM. Numerical simulation of gas-liquid–solid flows using a combined front tracking and discrete particle method. *Chem Eng Sci.* 2005;60:2188–2198.
64. Hirt CW, Nichols, BD. Volume of fluid (VOF) method for the dynamics of free boundaries. *J Comput Phys.* 1981;39:201–225.
65. Harmathy TZ. Velocity of large drops and bubbles in media of infinite or restricted extent. *AIChE J.* 1960;6:281–288.
66. Brackbill, JU, Kothe DB, Zemach C. A continuum method for modeling surface tension. *J Comput Phys.* 1992;100:335–354.
67. Cundall PA, Strack ODL. A discrete numerical model for granular assemblies. *Geotechnique.* 1979;29:47–65.
68. Davison SM, Sharp KV. Transient simulations of the electrophoretic motion of a cylindrical particle through a 90° corner. *Microfluid Nanofluid.* 2008;4:409–418.
69. Einstein A. On the movement of small particles suspended in a stationary liquid demanded by the Molecular-Kinetic theory of heat. *Ann Phys.* 1905;17:549–560.
70. Fluent 6.3.26 Users' Guide. Fluent Inc., Lebanon, NH; 2006.
71. Cherlo SKR, Kariveti S, Pushpavanam S. Experimental and numerical investigations of two-Phase (liquid— liquid) flow behavior in rectangular microchannels. *Ind Eng Chem Res.* 2010;49:893–899.
72. Dombrowski N, Foumeny EA, Ookawara S, Riza A. The influence of Reynolds number on the entry length and pressure drop for laminar pipe flow. *Can J Chem Eng.* 1993;71:472–476.

73. Spelt PDM. A level set approach for simulations of flows with multiple moving contact lines with hysteresis. *J Comput Phys*. 2005;207:389–404.
74. Renardy M, Renardy Y, Li J. Numerical simulation of moving contact line problems using a volume-of-fluid method. *J Comput Phys*. 2001;171:243–263.
75. Gerlach D, Alleborn N, Buwa V, Durst F. Numerical simulation of periodic bubble formation at submerged orifices under constant inflow conditions. *Chem Eng Sci*. 2007;62:2109–2125.
76. Kashid MN, Renken A, Kiwi-Minsker L. CFD modelling of liquid-liquid multiphase microstructured reactor: Slug flow generation. *Chem Eng Res Des*. 2010;88:362–388.
77. Sbrizzai F, Faraldi P, Soldati A. Appraisal of three-dimensional numerical simulation for sub-micron particle deposition in a micro-porous ceramic filter. *Chem Eng Sci*. 2005;60:6551–6563.
78. Li S-Q, Marshall JS. Discrete element simulation of micro-particle deposition on a cylindrical fiber in an array. *J Aerosol Sci*. 2007;38:1031–1046.
79. Fairbrother F, Stubbs, AE. Studies in electroendosmosis-VI. The"bubble tube" method of measurement. *J Chem Soc*. 1935;1:527–529.
80. Jin Y, Zhu J, Wang Z, Yu Z. Fluidization Engineering Principles. Beijing: Tsinghua University Press; 2001.
81. Tsuchiya K, Furumoto A, Fan L—S, Zhang J. Suspension viscosity and bubble rise velocity in liquid–solid fluidized beds. *Chem Eng Sci*. 1997;52:3053–3066.
82. Yang GQ, Du B, Fan L—S. Bubble formation and dynamics in gas-liquid–solid fluidization-A review. *Chem Eng Sci*. 2007;62:2–27.
83. Fu T, Ma Y, Funfschilling D, Zhu C, Li HZ. Squeezing-to-dripping transition for bubble formation in a microfluidic T-junction. *Chem Eng Sci*. 2010;65:3739–3748.
84. Xu JH, Luo GS, Li SW, Chen GG. Shear force induced monodisperse droplet formation in a microfluidic device by controlling wetting properties. *Lab Chip*. 2006;6:131–136.
85. Tan L, Liu M, Hu Z. Hydrodynamics and adsorption mass transfer in a novel gas- liquid -solid circulating fluidized bed adsorber. *Ind Eng Chem Res*. 2011;50:3598–3612.

Manuscript received Aug. 25, 2012, and revision received Nov. 4, 2012.